

# Magneto-optical conductivity in Graphene

V P Gusynin<sup>1</sup>, S G Sharapov<sup>2</sup> and J P Carbotte<sup>2</sup>

<sup>1</sup> Bogolyubov Institute for Theoretical Physics, 14-b Metrologicheskaya Street, Kiev, 03143, Ukraine

<sup>2</sup> Department of Physics and Astronomy, McMaster University, Hamilton, Ontario, Canada, L8S 4M1

E-mail: [vgusynin@bitp.kiev.ua](mailto:vgusynin@bitp.kiev.ua)

E-mail: [carbotte@mcmaster.ca](mailto:carbotte@mcmaster.ca)

E-mail: [sharapov@bitp.kiev.ua](mailto:sharapov@bitp.kiev.ua)

**Abstract.** Landau level quantization in graphene reflects the Dirac nature of its quasiparticles and has been found to exhibit an unusual integer quantum Hall effect. In particular the lowest Landau level can be thought as shared equally by electrons and holes and this leads to characteristic behaviour of the magneto-optical conductivity as a function of frequency  $\Omega$  for various values of the chemical potential  $\mu$ . Particular attention is paid to the optical spectral weight under various absorption peaks and its redistribution as  $\mu$  is varied. We also provide results for magnetic field  $B$  as well as chemical potential sweeps at selected fixed frequencies which can be particularly useful for possible measurements in graphene. Both diagonal and Hall conductivity are considered.

PACS numbers: 78.20.Ls, 73.43.Qt, 81.05.Uw

Submitted to: *J. Phys.: Condens. Matter*

## 1. Introduction

Recent experimental studies [1, 2] of the dynamics of electrons and holes in graphene (a single atomic layer of graphite [3]) have revealed unusual behaviour related to the Dirac nature of its quasiparticles. Two dimensional graphene has a honeycomb lattice structure with two atoms per unit cell. Its band structure consists of two inequivalent pairs of cones with apex at the Brillouin zone corners. For zero chemical potential the lower energy cones are completely filled and the upper empty. In a graphene device an applied gate voltage can be used to introduce electrons in the upper band or, by voltage reversal, holes in the lower band (cones).

The quasiparticles in graphene obey Dirac [4, 5] rather than the Schrödinger equation and this has profound implications for their dynamics. The unconventional quantum Hall effect was expected theoretically [6, 7, 8, 9, 10] and recently observed [1, 2] to have half (divided by spin and valley degeneracy) rather than integer filling factors. The predicted phase shift of  $\pi$  in the de Haas van Alphen [11, 12, 13] and Shubnikov de Haas [14] oscillations was also seen experimentally [1, 2]. Another feature related to the Dirac-like character of the carriers in graphene seen in the dc measurements is a finite effective cyclotron mass for the massless Dirac quasiparticles which varies as the square root of the number of carriers [11, 14, 1, 2].

In this paper we consider the magneto-optical conductivity of graphene. Work without a magnetic field includes the calculations of Ando, Zheng and Suzuura [15] who considered the effect on the frequency dependent conductivity of short- and long-range scatterers in a self consistent Born approximation. More recent work [16] describes several anomalous properties of the microwave conductivity of graphene with, as well as without magnetic field. These properties are directly related to the Dirac nature of the quasiparticles. Several analytic formulas for the longitudinal as well as Hall ac conductivity are given in the paper [8]. They also present extensive results for dc properties and preliminary data on the real part of  $\sigma_{xx}(\Omega)$  vs  $\Omega$  in the optical region. Another extensive work by Peres et al. [9] on the ac conductivity in graphene treats localized impurities in a self-consistent fashion as well as extended edge and grain boundaries including also effects of electron-electron interactions and self-doping.

In this paper we follow most closely Ref. [8] which we extend in several directions. An aim is to provide simpler analytic formulae which should prove useful in the analysis of experiment and check on their accuracy. Another is to consider magnetic field as well as chemical potential sweeps possible in graphene field effect transistor devices [1, 2, 3, 17]. Recent work by Li et al. in organic metals [18] has demonstrated that the ac measurements are also possible in such devices. Consistent with our aim, we consider impurities only in simplified scattering rate model and neglect real part renormalizations although these could easily be included if wished. While the renormalization effects beyond those included in this simplified model might become important for the interpretation of future experiment, we point out that so far the free quasiparticle model with associated transport lifetime has been remarkably successful

in understanding the dc results of Refs. [1, 2].

In Sec. 2 we relate the magneto-optical conductivity tensor to the Dirac fermionic Green's function through Kubo formula. The general formulas obtained can be greatly simplified and closed form expressions are obtained in two cases. In general the fermionic self-energy can depend on energy and Landau level index as well as temperature and value of the external magnetic field  $B$ . Under the assumption that variations with Landau level index  $n$  can be neglected, the sum over transitions between neighboring Landau levels can be carried out explicitly and a closed form expression is obtained for conductivity in terms of digamma function. A single integral over an internal frequency remains. The expression obtained is suitable for calculations of the ac conductivity for any value of temperature, chemical potential and magnetic field. Its microwave frequency limit has been used to describe properties of graphene in Ref. [16]. In the case when energy dependence of the fermionic self-energy can be neglected, the internal integration over energy can be done and what remains is the sum over the Landau level index  $n$  of Lorentzian forms multiplied by thermal factors and algebraic weighting factors. The weighting factors depend on the Landau level energies as well as the excitonic gap (see e.g. Refs. [19, 20, 21]) should one wish to include this possibility. When we compare numerical results obtained from Lorentzian model and from the previous more general expressions in the limit of constant scattering rate, we find good quantitative agreement between the two. This provides support for the analysis of experimental data [22]. In Sec. 2.3 we consider the low field limit for the Lorentzian model derived in Sec. 2.2 and establish its correspondence with previously known results. In Sec. 3.1 we present the numerical results for the real part of the diagonal conductivity as a function of photon energy  $\Omega$  for fixed value of magnetic field and various values of chemical potential. We also provide results for fixed photon energy while sweeping either chemical potential or external magnetic field which should prove useful in comparing with experiments. The effect of opening of an excitonic gap on the absorption lines is described. In Sec. 3.2 a discussion of optical spectral weight redistribution by the magnetic field is given. Section 3.3 is structured in parallel to Sec. 3.1 but deals with the absorptive part of the off-diagonal Hall magneto-optical conductivity. Discussion and conclusions are given in Sec. 4. Some of the algebra needed in this work is found in an Appendix A.

## 2. Analytic expressions for optical conductivity

The optical conductivity tensor is calculated using the Kubo formula

$$\sigma_{ij}(\Omega) = \frac{\Pi_{ij}^R(\Omega + i0)}{i\Omega}, \quad (1)$$

where  $\Pi_{ij}^R(\Omega)$  is the retarded current-current correlation function which in the bubble approximation is given by

$$\Pi_{ij}(\Omega+i0) = e^2 v_F^2 \int_{-\infty}^{\infty} d\omega d\omega' \frac{n_F(\omega') - n_F(\omega)}{\omega - \omega' - \Omega - i0} \int \frac{d^2k}{(2\pi)^2} \text{tr} [\gamma^i A(\omega, \mathbf{k}) \gamma^j A(\omega', \mathbf{k})], \quad i = 1, 2 \quad (2)$$

where  $n_F(\omega)$  is the Fermi distribution function  $n_F(\omega) = 1/[\exp((\omega - \mu)/T) + 1]$ ,  $\text{tr}$  not only takes care of the  $4 \times 4$   $\gamma$  matrices [ $\gamma^\nu = \sigma_3 \otimes (\sigma_3, i\sigma_2, -i\sigma_1)$ ], but includes also the summation over flavour (spin) index. Here

$$A(\omega, \mathbf{k}) = e^{-\frac{c\mathbf{k}^2}{|eB|}} \sum_{n=0}^{\infty} \frac{(-1)^n \Gamma_n(\omega)}{2\pi M_n} \left[ \frac{(\gamma^0 M_n + \Delta) f_1(\mathbf{k}) + f_2(\mathbf{k})}{(\omega - M_n)^2 + \Gamma_n^2(\omega)} + \frac{(\gamma^0 M_n - \Delta) f_1(\mathbf{k}) - f_2(\mathbf{k})}{(\omega + M_n)^2 + \Gamma_n^2(\omega)} \right] \quad (3)$$

is the spectral function (decomposed over Landau levels) associated with the translation invariant part of the Dirac fermion Green's function in an external magnetic field  $\mathbf{B}$  applied perpendicular to the plane along the positive  $z$  direction (see e.g. Refs. [21, 11]). In Eq. (3)

$$f_1(\mathbf{k}) = 2 \left[ P_- L_n \left( \frac{2c\mathbf{k}^2}{|eB|} \right) - P_+ L_{n-1} \left( \frac{2c\mathbf{k}^2}{|eB|} \right) \right], \quad f_2(\mathbf{k}) = 4v_F \mathbf{k} \gamma L_{n-1}^1 \left( \frac{2c\mathbf{k}^2}{|eB|} \right) \quad (4)$$

with  $P_\pm = (1 \pm i\gamma^1 \gamma^2 \text{sgn}(eB))/2$  being projectors and  $L_n^\alpha(z)$  the generalized Laguerre polynomials. By definition,  $L_n(z) \equiv L_n^0(z)$  and  $L_{-1}^\alpha(z) \equiv 0$ . The energies of the relativistic Landau levels in Eq. (3) are

$$E_n = \pm M_n, \quad M_n = \sqrt{\Delta^2 + 2nv_F^2 |eB|/c}, \quad (5)$$

where the energy scale associated with the magnetic field expressed in the units of temperature reads

$$\frac{eBv_F^2}{c} \rightarrow \frac{eB\hbar v_F^2}{c} \frac{1}{k_B^2} = 8.85 \times 10^{-8} \text{K}^2 v_F^2 (\text{m/s}) B(T), \quad (6)$$

where  $v_F$  is the Fermi velocity in graphene given in m/s and the field  $B$  is given in Tesla. In the following we set  $\hbar = k_B = 1$ , and in some places  $e = c = 1$ , unless stated explicitly otherwise. For the numerical calculations we use the value  $v_F \approx 10^6 \text{m/s}$  [1, 2] which leads to the relationship  $eB \rightarrow (8.85 \times 10^4 \text{K}^2) B(T)$ . We consider relatively low fields  $B \lesssim 17 \text{T}$ , where spin splitting is unresolved [23], so that we can assume that the above mentioned summation over flavor index simply gives  $N_f = 2$  in all expressions below. The Landau level energies (5) include also an excitonic gap  $\Delta$ . The physical meaning of this singlet excitonic gap is directly related to the electron density imbalance between the A and B sublattices of the bi-particle hexagonal lattice of graphene [19, 20] and there are strong indications [24] that it was indeed observed in recent experiments [23, 25]. We will see here that optical measurements done on graphene can be very useful in investigations of the excitonic gap.

Finally, the scattering rate  $\Gamma_n(\omega)$  is expressed via the retarded fermion self-energy,  $\Gamma_n(\omega) = -\text{Im}\Sigma_n^R(\omega)$  which in general depends on the energy, temperature, field and the Landau levels index  $n$ . This self-energy, which in general has also a real part, has to be determined self-consistently from the Schwinger-Dyson equation. This equation can be solved analytically [20] and numerically as was done in Refs. [6, 9]. In our paper we consider  $\Gamma_n(\omega)$  as a phenomenological parameter for the two cases: (i)  $\Gamma(\omega) = \Gamma_n(\omega)$  is independent of the Landau level index  $n$  and (ii)  $\Gamma_n = \Gamma_n(\omega)$  is independent of the energy  $\omega$ . Under these assumptions the optical conductivity can be studied analytically.

### 2.1. Frequency dependent scattering rate

Assuming that  $\Gamma_n(\omega)$  is independent of the Landau level index, i.e.  $\Gamma(\omega) = \Gamma_n(\omega)$ , one can calculate the sum over Landau levels and express the diagonal ac conductivity in the closed form [8]

$$\text{Re } \sigma_{xx}(\Omega) = \frac{e^2 N_f}{4\pi^2 \Omega} \int_{-\infty}^{\infty} d\omega [n_F(\omega) - n_F(\omega')] \text{Re} \left\{ \frac{2B}{\Delta^2 - (\tilde{\omega} + i\Gamma)^2} [\Xi_1(-B) - \Xi_2(-B)] \right. \\ \left. + [\Xi_1(-B) + \Xi_1(+B) - \Xi_2(-B) - \Xi_2(+B)] \psi \left( \frac{\Delta^2 - (\tilde{\omega} + i\Gamma)^2}{2B} \right) + (\tilde{\omega} \leftrightarrow \tilde{\omega}', \Gamma \leftrightarrow \Gamma') \right\}. \quad (7)$$

Here  $\psi$  is the digamma function, we denoted  $B \equiv v_F^2 |eB|/c$ , and also included the renormalization of energy caused by the real part of self-energy  $\tilde{\omega}(\omega) = \omega - \text{Re } \Sigma(\tilde{\omega})$ ,  $\tilde{\omega}' = \tilde{\omega}(\omega + \Omega)$ ,  $\Gamma = \Gamma(\tilde{\omega})$ ,  $\Gamma' = \Gamma(\tilde{\omega}')$  and introduced the following short-hand notations

$$\Xi_1(\pm B) \equiv \Xi_1(\tilde{\omega}, \tilde{\omega}', \Gamma, \Gamma', \pm B) = \frac{(\tilde{\omega}' + i\Gamma')(\tilde{\omega} + i\Gamma) - \Delta^2}{[\tilde{\omega} - \tilde{\omega}' + i(\Gamma - \Gamma')][\tilde{\omega} + \tilde{\omega}' + i(\Gamma + \Gamma')] \pm 2B}, \\ \Xi_2(\pm B) \equiv \Xi_2(\tilde{\omega}, \tilde{\omega}', \Gamma, \Gamma', \pm B) = \frac{(\tilde{\omega}' - i\Gamma')(\tilde{\omega} + i\Gamma) - \Delta^2}{[\tilde{\omega} - \tilde{\omega}' + i(\Gamma + \Gamma')][\tilde{\omega} + \tilde{\omega}' + i(\Gamma - \Gamma')] \pm 2B}. \quad (8)$$

The advantage of Eq. (7) is that the  $\psi$  function contains the contribution to conductivity from *all* transitions between neighboring Landau levels. An infinite number of these transitions need to be taken into account when the limit  $B \rightarrow 0$  is considered, so that the zero field limit is easily treatable [8] on the base of Eq. (7). Another important feature of Eq. (7) is that we kept the frequency dependent impurity scattering rate  $\Gamma(\omega)$  which allows us to investigate its influence on the shape of the Drude peak [16].

Although in our work we will mostly use Eq. (7) for the numerical computations of the diagonal conductivity, there is a possibility to derive simple approximate expressions for the diagonal and Hall conductivities which turn out to be very useful when one is interested in the resonance peaks of these conductivities in the infrared region.

### 2.2. Landau level index dependent scattering rate and magneto-optical Lorentzian model

For analyzing experimental data it is very useful to have a magneto-optical Lorentzian model for the complex conductivity,  $\sigma_{\pm}(\Omega) = \sigma_{xx}(\Omega) \pm i\sigma_{xy}(\Omega)$  due to inter- and intraband Landau level transitions [26]. For the case of Dirac fermions it is considered in Appendix A, whereof we obtain the complex diagonal conductivity

$$\sigma_{xx}(\Omega) = -\frac{e^2 v_F^2 |eB|}{2\pi c i} \sum_{n=0}^{\infty} \left\{ \left( 1 - \frac{\Delta^2}{M_n M_{n+1}} \right) ([n_F(M_n) - n_F(M_{n+1})] + [n_F(-M_{n+1}) - n_F(-M_n)]) \right. \\ \times \left( \frac{1}{M_n - M_{n+1} + \Omega + i(\Gamma_n + \Gamma_{n+1})} - \frac{1}{M_n - M_{n+1} - \Omega - i(\Gamma_n + \Gamma_{n+1})} \right) \frac{1}{M_{n+1} - M_n} \\ \left. + \left( 1 + \frac{\Delta^2}{M_n M_{n+1}} \right) ([n_F(-M_n) - n_F(M_{n+1})] + [n_F(-M_{n+1}) - n_F(M_n)]) \frac{1}{M_{n+1} + M_n} \right\} \quad (9)$$

$$\times \left( \frac{1}{M_n + M_{n+1} + \Omega + i(\Gamma_n + \Gamma_{n+1})} - \frac{1}{M_n + M_{n+1} - \Omega - i(\Gamma_n + \Gamma_{n+1})} \right) \Bigg\},$$

and the complex Hall conductivity

$$\begin{aligned} \sigma_{xy}(\Omega) &= \frac{e^2 v_F^2 e B}{2\pi c} \sum_{n=0}^{\infty} ([n_F(M_n) - n_F(M_{n+1})] - [n_F(-M_{n+1}) - n_F(-M_n)]) \\ &\times \left\{ \left( 1 - \frac{\Delta^2}{M_n M_{n+1}} \right) \frac{1}{M_{n+1} - M_n} \right. \\ &\times \left( \frac{1}{M_n - M_{n+1} + \Omega + i(\Gamma_n + \Gamma_{n+1})} + \frac{1}{M_n - M_{n+1} - \Omega - i(\Gamma_n + \Gamma_{n+1})} \right) \\ &- \left( 1 + \frac{\Delta^2}{M_n M_{n+1}} \right) \frac{1}{M_{n+1} + M_n} \\ &\times \left. \left( \frac{1}{M_n + M_{n+1} + \Omega + i(\Gamma_n + \Gamma_{n+1})} + \frac{1}{M_n + M_{n+1} - \Omega - i(\Gamma_n + \Gamma_{n+1})} \right) \right\}. \end{aligned} \quad (10)$$

In deriving Eqs. (9), (10) we assumed that the impurity scattering rate is independent of the energy  $\omega$ , but kept its dependence on the Landau level index  $n$ . This assumption allows us to eliminate the integration over  $\omega$  which is present in Eq. (7). To preserve the Landau index dependence, the sum over transitions between neighboring Landau levels is retained in Eqs. (9), (10).

Based on Eqs. (9), (10) one can easily write down separate expressions for  $\text{Re } \sigma_{xx}(\Omega)$ ,  $\text{Im } \sigma_{xx}(\Omega)$ ,  $\text{Re } \sigma_{xy}(\Omega)$ ,  $\text{Im } \sigma_{xy}(\Omega)$  and verify that diagonal and off-diagonal conductivities satisfy Kramers-Kronig relations. A big advantage of Eqs. (9), (10) is that they are more suitable for numerical computations and it is sufficient to include only a few terms in the sum even in relatively low magnetic field. Also they are useful for the description of the resonance peaks when the Landau level index dependence is more important than the energy dependence of the scattering rate which is included in Eq. (7).

All figures in this paper were computed for  $\Gamma = \text{const}$ , so that for calculation of the diagonal conductivity we used Eq. (7) and checked that it gives almost identical results to Eq. (9). Since the corresponding full expression for the optical Hall conductivity derived in Ref. [8] is rather difficult for numerical calculations, in the present paper we compute all results for the Hall conductivity using Eq. (10). In the case of Landau level index independent width,  $\Gamma_n = \text{const}$ , Eqs. (9), (10) acquire an even simpler form

$$\begin{aligned} \sigma_{xx}(\Omega) &= \frac{e^2 v_F^2 |eB| (\Omega + 2i\Gamma)}{\pi c i} \\ &\times \sum_{n=0}^{\infty} \left\{ \left( 1 - \frac{\Delta^2}{M_n M_{n+1}} \right) \frac{[n_F(M_n) - n_F(M_{n+1})] + [n_F(-M_{n+1}) - n_F(-M_n)]}{(M_{n+1} - M_n)^2 - (\Omega + 2i\Gamma)^2} \frac{1}{M_{n+1} - M_n} \right. \\ &+ \left. \left( 1 + \frac{\Delta^2}{M_n M_{n+1}} \right) \frac{[n_F(-M_n) - n_F(M_{n+1})] + [n_F(-M_{n+1}) - n_F(M_n)]}{(M_{n+1} + M_n)^2 - (\Omega + 2i\Gamma)^2} \frac{1}{M_{n+1} + M_n} \right\} \end{aligned} \quad (11)$$

and

$$\sigma_{xy}(\Omega) = -\frac{e^2 v_F^2 e B}{\pi c} \sum_{n=0}^{\infty} ([n_F(M_n) - n_F(M_{n+1})] - [n_F(-M_{n+1}) - n_F(-M_n)]) \quad (12)$$

$$\times \left\{ \left( 1 - \frac{\Delta^2}{M_n M_{n+1}} \right) \frac{1}{(M_{n+1} - M_n)^2 - (\Omega + 2i\Gamma)^2} + \left( 1 + \frac{\Delta^2}{M_n M_{n+1}} \right) \frac{1}{(M_{n+1} + M_n)^2 - (\Omega + 2i\Gamma)^2} \right\}.$$

One can see that the conductivity  $\sigma_{xx}(\Omega, \mu)$  is even function of  $\mu$  while  $\sigma_{xy}(\Omega, \mu)$  is an odd one.

### 2.3. Low field limit of the magneto-optical Lorentzian model

Now we check that Eqs.(11), (12) reproduce correctly the limit  $B \rightarrow 0$ . Introducing the continuum variable  $\omega$  instead of  $M_n$  given by Eq. (5) and replacing the sum over  $n$  by the integral, we obtain

$$\sigma_{xx}(\Omega) = -\frac{2ie^2(\Omega + 2i\Gamma)}{h} \left[ \frac{1}{(\Omega + 2i\Gamma)^2} \int_{\Delta}^{\infty} d\omega \frac{\omega^2 - \Delta^2}{\omega} \left( \frac{\partial n_F(\omega)}{\partial \omega} - \frac{\partial n_F(-\omega)}{\partial \omega} \right) - \int_{\Delta}^{\infty} d\omega \frac{\omega^2 + \Delta^2}{\omega^2} \frac{n_F(-\omega) - n_F(\omega)}{(\Omega + 2i\Gamma)^2 - 4\omega^2} \right] \quad (13)$$

and

$$\sigma_{xy}(\Omega) = \frac{e^2 v_F^2 e B}{\pi c} \int_{\Delta}^{\infty} d\omega \left( \frac{\partial n_F(\omega)}{\partial \omega} + \frac{\partial n_F(-\omega)}{\partial \omega} \right) \times \left[ -\frac{\omega^2 - \Delta^2}{\omega^2} \frac{1}{(\Omega + 2i\Gamma)^2} + \frac{\omega^2 + \Delta^2}{\omega^2} \frac{1}{4\omega^2 - (\Omega + 2i\Gamma)^2} \right], \quad (14)$$

where we restored Planck constant  $h = 2\pi\hbar$  in the overall prefactor. Here the terms with the factor  $(\omega^2 - \Delta^2)/\omega^2$  are intraband and the terms containing the factor  $(\omega^2 + \Delta^2)/\omega^2$  are interband. The expressions (13) and (14) are obtained under the condition  $\sqrt{\hbar|eB|v_F^2/c} \ll \Gamma$ . The intraband term of Eq. (13) can be written in the familiar Drude form

$$\sigma_{xx}^{\text{Drude}}(\Omega) = \frac{2e^2}{h} \int_{-\infty}^{\infty} d\omega \left( -\frac{\partial n_F(\omega)}{\partial \omega} \right) \frac{1}{2\Gamma - i\Omega} \frac{(\omega^2 - \Delta^2)\theta(\omega^2 - \Delta^2)}{|\omega|} \quad (15)$$

which for  $\Delta = 0$  reduces to Eq. (2) of Ref. [16]. The whole expression (13) which includes the interband term, also reduces to the other limiting cases considered in Refs. [16, 27]. In particular, an unusual feature of graphene is that in the high frequency limit the interband contribution is a constant,

$$\sigma_{xx}(\Omega) \simeq \frac{\pi e^2}{2h}, \quad \Omega \gg \mu, \Delta, T. \quad (16)$$

Here to rely on the linearized Dirac approximation we assumed that  $\Omega$  is still well below a large band edge.

The real part of the Hall conductivity (14) for  $\Omega = \Delta = T = 0$  reduces to the expression

$$\sigma_{xy}(\Omega = 0) = -\frac{e^2 v_F^2 e B \text{sgn} \mu}{4\pi c \Gamma^2}, \quad \sqrt{\hbar|eB|v_F^2/c} \ll \Gamma \ll |\mu| \quad (17)$$

which is in agreement with Eq. (4.3) of Ref. [8]. On the other hand, in the high frequency limit Eq. (14) gives

$$\sigma_{xy}(\Omega) = \frac{e^2 v_F^2 e B}{\pi c (\hbar \Omega)^2} \left[ \tanh \frac{\mu + \Delta}{2T} + \tanh \frac{\mu - \Delta}{2T} \right], \quad \Omega \rightarrow \infty. \quad (18)$$

This behavior also follows from Eq. (10) which is valid in an arbitrary field  $B$ . Interestingly, expression (18) is sensitive to the relationship between  $|\mu|$  and  $\Delta$  and this feature can be used for the gap detection [see the discussion of Figs. 4 and 9 below]. Using Eqs. (16) and (18) we obtain the weak field optical Hall resistivity

$$\begin{aligned} \rho_{xy}(\Omega) &= - \frac{\sigma_{xy}(\Omega)}{\sigma_{xx}^2(\Omega) + \sigma_{xy}^2(\Omega)} \\ &= - \frac{16 v_F^2 B}{\pi e c \Omega^2} \left[ \tanh \frac{\mu + \Delta}{2T} + \tanh \frac{\mu - \Delta}{2T} \right], \quad \Omega \gg \mu, \Delta, T. \end{aligned} \quad (19)$$

Accordingly, the high frequency optical Hall coefficient for  $\Delta = 0$  and  $T \rightarrow 0$

$$R_H(\Omega) = \frac{\rho_{xy}(\Omega)}{B} = - \frac{32 v_F^2}{\pi e c \Omega^2} \text{sgn}(\mu) \quad (20)$$

contains the information on the value of the Fermi velocity in graphene.

Finally, the imaginary part of  $\sigma_{xy}(\Omega)$  which follows from Eq. (14) is given by the expression

$$\begin{aligned} \text{Im } \sigma_{xy}(\Omega) &= \frac{4e^2 v_F^2 e B \Gamma \Omega}{\pi c} \int_{\Delta}^{\infty} d\omega \left( \frac{\partial n_F(\omega)}{\partial \omega} + \frac{\partial n_F(-\omega)}{\partial \omega} \right) \\ &\quad \left[ \frac{1}{(\Omega^2 - 4\Gamma^2)^2 + 16\Omega^2\Gamma^2} + \frac{1}{(4\Gamma^2 - \Omega^2 + 4\Gamma^2)^2 + 16\Omega^2\Gamma^2} \right] \end{aligned} \quad (21)$$

which in high frequency limit becomes

$$\text{Im } \sigma_{xy}(\Omega) \simeq - \frac{4e^2 v_F^2 e B \Gamma}{\pi c (\hbar \Omega)^3} \left( \tanh \frac{\mu + \Delta}{2T} + \tanh \frac{\mu - \Delta}{2T} \right), \quad \Omega \rightarrow \infty. \quad (22)$$

The last equation shows that in this limit real part of  $\sigma_{xy}$  given by Eq. (18) is the leading term.

### 3. Results for optical conductivity

#### 3.1. Diagonal conductivity

In Fig. 1 we show the results based on a numerical evaluation of the full equation (7) for the real part of the longitudinal conductivity  $\text{Re } \sigma_{xx}(\Omega)$  in units  $e^2/h$  as a function of frequency in units of  $\text{cm}^{-1}$ . Except for the long dashed (red) curve which was obtained in the limit of vanishing external magnetic field (namely  $B = 10^{-4}\text{T}$ ) and is included for comparison, the other three curves are for  $B = 1\text{T}$ . They differ in value of the chemical potential  $\mu$ . In all cases the temperature  $T = 10\text{K}$ , the impurity scattering  $\Gamma = 15\text{K}$ , and the excitonic gap  $\Delta = 0$ . For reference in scrutinizing the curves, the frequency of the  $n = 1$  Landau level,  $\Omega_1 = M_1(\Delta = 0) = 294\text{cm}^{-1}[423\text{K}]$ ,



$\Omega_2 = M_2(\Delta = 0) = 415.8\text{cm}^{-1}[598\text{ K}]$  and  $\Omega_3 = M_3(\Delta = 0) = 509.2\text{cm}^{-1}[733\text{ K}]$ , so that for the dash-dotted (black) curve  $\mu$  falls below the energy of the  $n = 1$  level (see left side of Fig. 2 (c)) ‡, for the solid (blue) curve it falls between  $n = 1$  and  $n = 2$  levels (see middle of Fig. 2 (c)), and for the short dashed (green) it is between  $n = 2$  and  $n = 3$  (right side of Fig. 2 (c)). The energies of the peaks are  $M_1, M_1 + M_2, M_2 + M_3$ , etc. and  $M_2 - M_1, M_3 - M_2$ , etc. Note that the position and the intensity of the last two peaks in Fig. 1 (largest frequency  $\Omega$ ) remains the same for all chosen values of the chemical potential  $\mu$ . When  $\mu$  falls between  $M_2$  and  $M_3$  [short dashed (green) curve]

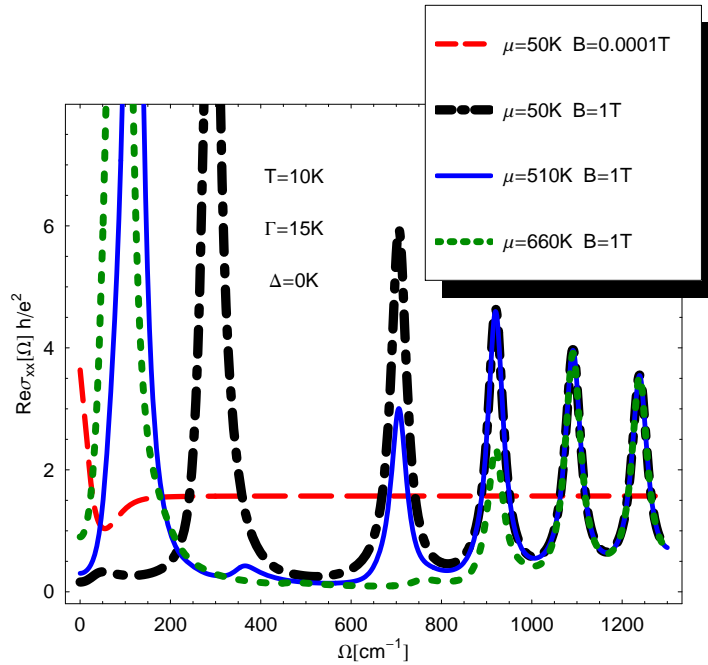


**Figure 1.** (Colour online) Real part of the longitudinal conductivity,  $\text{Re}\sigma_{xx}(\Omega)$  in units of  $e^2/h$  vs frequency  $\Omega$  in  $\text{cm}^{-1}$  for temperature  $T = 10\text{K}$ , scattering rate  $\Gamma = 15\text{K}$ . Long dashed, the chemical potential  $\mu = 50\text{K}$  and the magnetic field  $B = 10^{-4}\text{T}$ , dash-dotted  $\mu = 50\text{K}$  and  $B = 1\text{T}$ , solid  $\mu = 510\text{K}$  and  $B = 1\text{T}$ , short dashed  $\mu = 660\text{K}$  and  $B = 1\text{T}$ .

the intensity in the third last peak has dropped to half the value it has in solid (blue) curve, while the fourth last peak has merged into a low intensity background, as has the fifth last, which is seen only in the dash-dotted curve. Also a new peak has appeared at  $M_3 - M_2$  which was not present in the dash-dotted curve. Similarly for  $\mu$  between  $M_1$  and  $M_2$  [solid (blue) curve] the intensity of the fourth highest energy peak has dropped to half the intensity it has in the dash-dotted curve and the peak at  $M_1$  is entirely missing, having merged into the low intensity background. A new peak has appeared at  $M_2 - M_1$ . Finally when  $\mu$  is below  $M_1$  (dash-dotted curve) there is no peak below  $M_1$  and the line at  $M_1$  always has full intensity. *Whatever the value of  $\mu$  this line will*

‡ We recall that the conversion rule from the frequency in  $\text{cm}^{-1}$  to the energy in Kelvins is  $\Omega[\text{K}] = 1.4387\text{K} \cdot \text{cm}\Omega[\text{cm}^{-1}]$ .

never be seen to half its intensity and this is the hallmark of the Dirac nature of the quasiparticles. A schematic which helps us understand the behaviour of the absorption lines that we have just described is given in Fig. 2 (c). On the left of the figure we show the energies of the Landau levels  $E_n = \pm M_n$  of Eq. (5) as solid (red) dots along with their quantum numbers  $n = 0, 1, 2, \dots$ . The Dirac cones which come in pairs, with the positive and negative energies and exist at  $\mathbf{K}$  and  $\mathbf{K}'$  points in graphene Brillouin zone are also shown. The three values of chemical potential considered in Fig. 2 (c) are shown in heavy solid (violet) horizontal lines. The possible optical transitions in each case are indicated as vertical arrows and connect levels  $n$  to  $n \pm 1$  only. Moving from left to right we see first a single transition from  $E_0$  to  $E_1 = M_1$ , then a pair of interband from  $E_1 = -M_1$  to  $E_2 = M_2$  and  $E_2 = -M_2$  to  $E_1 = M_1$  followed by another pair from  $E_2 = -M_2$  to  $E_3 = M_3$  and  $E_3 = -M_3$  to  $E_2 = M_2$  etc. For the middle set of lines the first is an intraband transition from  $E_1 = M_1$  to  $E_2 = M_2$  followed by a single interband from  $E_1 = -M_1$  to  $E_2 = M_2$  and then a pair from  $E_2 = -M_2$  and  $E_3 = M_3$  and  $E_3 = -M_3$  to  $E_2 = M_2$  etc. Finally in the set of transitions at the right of the figure there is an intraband from  $E_2 = M_2$  to  $E_3 = M_3$  followed by a single interband from  $E_2 = -M_2$  to  $E_3 = M_3$  and a pair from  $E_3 = -M_3$  to  $E_4 = M_4$  and  $E_4 = -M_4$  to  $E_3 = M_3$  etc. This is precisely the pattern we have seen in Fig. 1. We note one more aspect of the anomalous line at the far left of the figure for the transition from  $n = 0$  to  $n = 1$  Landau level. It is the only line which cannot be unambiguously assigned to inter or intraband because the state at  $n = 0$  falls at the apex of the Dirac cones, where positive and negative energy cones meet and hence they share this state equally. This is further illustrated in Figs. 2 (a) and (b), where two sets of cones at  $\mathbf{K}$  and  $\mathbf{K}'$  are shown separately for the case of  $\Delta = 0$  in frame (a) and finite excitonic gap in frame (b). In this second case we see clearly that points  $\mathbf{K}$  and  $\mathbf{K}'$  react differently under a finite magnetic field. For the cone on the left  $n = 0$  level has moved to energy  $E_0 = -\Delta$  and for the cone on the right it has moved to  $E_0 = \Delta$ . Note that for the value of chemical potential shown as a solid horizontal (violet) line, the  $E_0 = -\Delta$  to  $E_1$  transition (vertical arrow) on the left is now definitely interband and the  $E_0 = \Delta$  to  $E_1$  on the right is intraband. The ambiguity in designation of the  $n = 0$  level present in the top frame (a) of Fig. 2 is lifted when the gap becomes finite.

The rather complicated pattern of behaviour just described can be understood simply from the mathematics of the previous section in the limit  $\Gamma \rightarrow 0$  and  $T \rightarrow 0$ . Taking  $\Delta = 0$ ,  $\mu \geq 0$ , and  $\Omega \geq 0$  one obtains from Eq. (A.12)

$$\begin{aligned} \text{Re } \sigma_{xx}(\Omega) = & \frac{e^2}{h} M_1^2 \frac{\pi}{2} \sum_{n=0}^{\infty} \left\{ [2 - n_F(M_n) - n_F(M_{n+1})] \frac{\delta(M_n + M_{n+1} - \Omega)}{M_n + M_{n+1}} \right. \\ & \left. + [n_F(M_n) - n_F(M_{n+1})] \frac{\delta(M_n - M_{n+1} + \Omega)}{M_{n+1} - M_n} \right\}. \end{aligned} \quad (23)$$

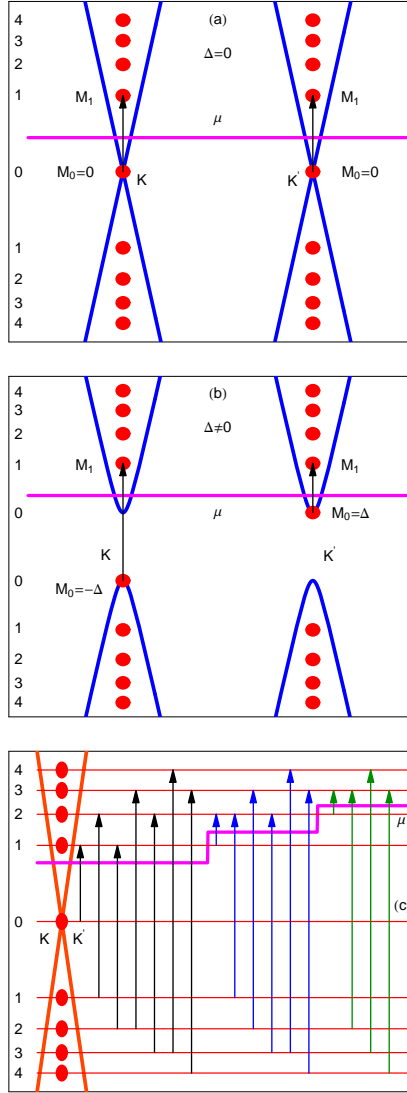


**Figure 2.** (Colour online) (a) Schematic representation of the two pairs of Dirac cones with apex at points  $\mathbf{K}$  (left) and  $\mathbf{K}'$  (right) in graphene Brillouin zone. The energies of the Landau levels are shown for index  $n = 0, \dots, 4$  as solid (red) circles for both positive and negative Dirac cones. The transition from  $n = 0$  to  $n = 1$  across the chemical potential shown as a thick horizontal (violet) line are for the case  $\Delta = 0$ . (b) Same as (a) but now there is a finite excitonic gap  $\Delta$ . (c) The pair of cones at points  $\mathbf{K}$  and  $\mathbf{K}'$  in the Brillouin zone (see panels (a) and (b)) are combined. Vertical arrows show allowed optical transitions between Landau levels for three values of the chemical potential. At left are the transitions when  $\mu$  is between  $n = 0$  and  $n = 1$ , in the middle between  $n = 1$  and  $n = 2$ , and the right between  $n = 2$  and  $n = 3$ . The first line in the left is different in that it is both inter (between two separate cones) and intra (within a given cone). The first line in all other series is intra and the shortest inter appears only once, while all others appear twice. Note that from Eq. (11)  $\sigma_{xx}(\Omega, \mu)$  is even in  $\mu$ , while from Eq. (12)  $\sigma_{xy}(\Omega, \mu)$  is odd in  $\mu$ .

For  $\mu \in ]M_N, M_{N+1}[$  the  $T = 0$  thermal factor

$$2 - n_F(M_n) - n_F(M_{n+1}) = \begin{cases} 0 & \text{for } n < N, \\ 1 & \text{for } n = N, \\ 2 & \text{for } n > N, \end{cases} \quad (24)$$

while

$$n_F(M_n) - n_F(M_{n+1}) = \begin{cases} 1 & \text{for } n = N, \\ 0 & \text{for } n \neq N. \end{cases} \quad (25)$$

The line in  $\text{Re } \sigma_{xx}(\Omega)$  with the frequency  $M_n + M_{n+1}$  occurs only for  $n \geq N$  with the others missing. Further the line with  $n = N$  has half of the weight it would have if it occurred in another case, namely,  $1/(M_n + M_{n+1})$ , while lines for  $n > N$  have full weight  $2/(M_n + M_{n+1})$ . Note that the lines with the frequency equal to the difference in Landau level energies have weight  $1/(M_{n+1} - M_n)$ . These lines are always present except for the case when  $\mu$  falls below  $M_1$  when the single line at  $M_1$  has weight  $2/M_1$ . In summary, we have seen in the above discussion that as  $\mu$  moves through higher and higher values of  $M_N$  the lines below  $N$  disappear into the background with a new line appearing at  $M_{N+1} - M_N$ . Further the line at  $n = N$  loses half its intensity while the others remain unaltered except for the special case when chemical potential falls below the Landau level  $M_1$ .

The pattern would be quite different if instead of  $M_n \sim \sqrt{n}$  the Landau level quantization was Schrödinger-like  $M_n = \omega_c(n + 1/2)$  with  $\omega_c$  being the cyclotron frequency. In this case the position of the line corresponding to the difference in Landau level energies (intraband) never shifts in energy. Further, the lines corresponding to the sum of the Landau level energies (interband) fall at regular energies intervals  $2\omega_c(n + 1)$ , namely  $2\omega_c, 4\omega_c, 6\omega_c, \dots$ . Furthermore as  $\mu$  increases through the energies of the various Landau levels all lines half their intensity before fading into the background and for  $\mu$  below the first level there is no line at  $\omega_c$ . There is also no ambiguity about whether a line is intra or interband as no level is shared between upper and lower cone.

In field effect devices the chemical potential in a graphene sheet can be changed by applying a gate voltage and this may be an ideal way to observe the effects just described. However, there is an alternative way to see the same effects. For any fixed value of chemical potential, the external magnetic field can be selected in such a way that  $\mu$  falls below the first Landau level or in between  $n = 1$  and  $n = 2$  etc. For appropriate choices of  $B$  [28] the curves for  $\text{Re } \sigma_{xx}(\Omega)$  can be made to behave exactly as in Fig. 1. To see this it is important that  $\Omega$  be divided by  $\sqrt{\hbar e B v_F^2 / c}$ , so that the lines remain fixed in normalized frequency and the vertical scale be divided by the same factor and multiplied by  $\Gamma$  to keep the dimensions the same. When this is done, the same pattern as seen in Fig. 1 emerges for this configuration corresponding to fixed  $\mu$  with several well chosen values of  $B$ .

We have found that the curves of Fig. 1 change very little as the chemical potential is varied within the limited range  $M_N$  to  $M_{N+1}$ . We have also verified that for the parameters used here  $T = 10\text{K}$ ,  $\Gamma = 15\text{K}$  the crossover from half intensity in the line

$M_N + M_{N+1}$  to near zero, i.e. merging into the background occurs rather abruptly in an energy range set by  $T$  and/or  $\Gamma$ . This is illustrated in Fig. 3 where we consider how the

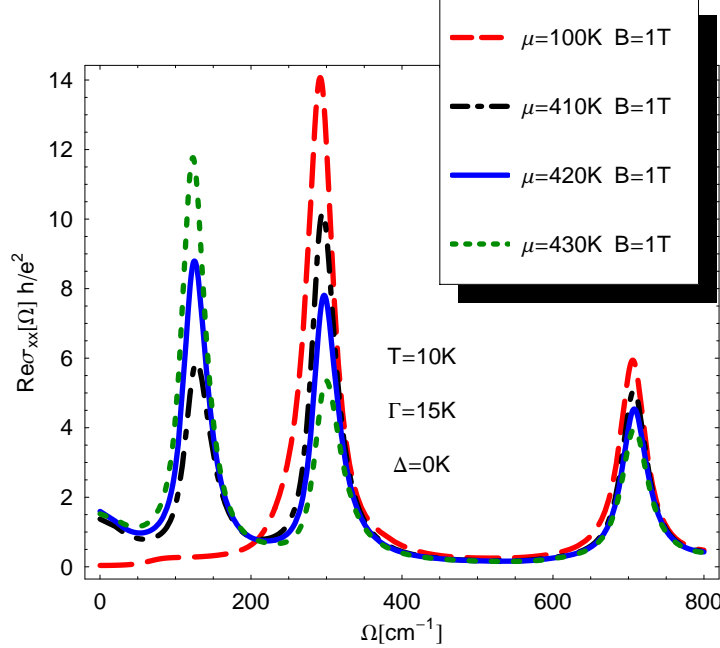


**Figure 3.** (Colour online) Real part of the longitudinal conductivity,  $\text{Re}\sigma_{xx}(\Omega)$  in units of  $e^2/h$  vs frequency  $\Omega$  in  $\text{cm}^{-1}$  for temperature  $T = 10\text{K}$ , scattering rate  $\Gamma = 15\text{K}$  and magnetic field  $B = 1\text{T}$  for 4 values of chemical potential. Long dashed  $\mu = 100\text{K}$ , dash-dotted  $\mu = 410\text{K}$ , solid  $\mu = 420\text{K}$ , short dashed  $\mu = 430\text{K}$ .

complete disappearance of the peak at  $\Omega = \Omega_1 = 294\text{cm}^{-1}$  ( $420\text{K}$ ) and the depletion of the next higher peak at  $710\text{cm}^{-1}$  towards half its initial value proceeds as the chemical potential  $\mu$  crosses through the energy of the  $n = 1$  Landau level [ $\Omega_1 = M_1(\Delta = 0)$ ]. The long dashed curve (red) is for  $\mu = 100\text{K}$  chosen to be well away from the crossover point of  $420\text{K}$  and is shown for comparison. The dash-dotted curve (black) is for  $\mu = 410\text{K}$  slightly below the crossover point, the solid curve (blue) is for  $\mu = 420\text{K}$  just at the crossover energy and the short dashed curve (green) is for  $\mu = 430\text{K}$  which spans  $\pm 10\text{K}$  on either side of  $\Omega_1$  which is much less than the level width of  $2\Gamma = 30\text{K}$ . As  $\mu$  increases through  $410\text{K}$  we note the growth of the peak at  $\Omega = 122\text{cm}^{-1}$ , the depletion towards zero value of the peak at  $294\text{cm}^{-1}$  and towards half its initial value of the next higher peak at  $710\text{cm}^{-1}$ . The complete transfer of spectral weight between the various peaks is completed for a rather small region of chemical potential variation about  $\Omega_1 = 294\text{cm}^{-1}$  ( $420\text{K}$ ) of order  $30\text{K}$  (not shown in the figure). After the crossover is complete, the pattern of the spectral weight distribution will remain unchanged until the chemical potential becomes close to the energy of the next Landau level. We would like to stress that although Fig. 3 is plotted using the full expression (7), we have verified that the results obtained using Eqs. (A.12) and (9) are practically identical.

Returning to Eqs. (23) to (25) we note that the optical spectral weight under a given

inter- or intraband line varies as the square root of  $B$  (see Eq. (32) and the discussion associated with it). This has been verified in the recent experiment of Sadowski *et al.* [29] on ultrathin epitaxial graphite samples [30, 31].

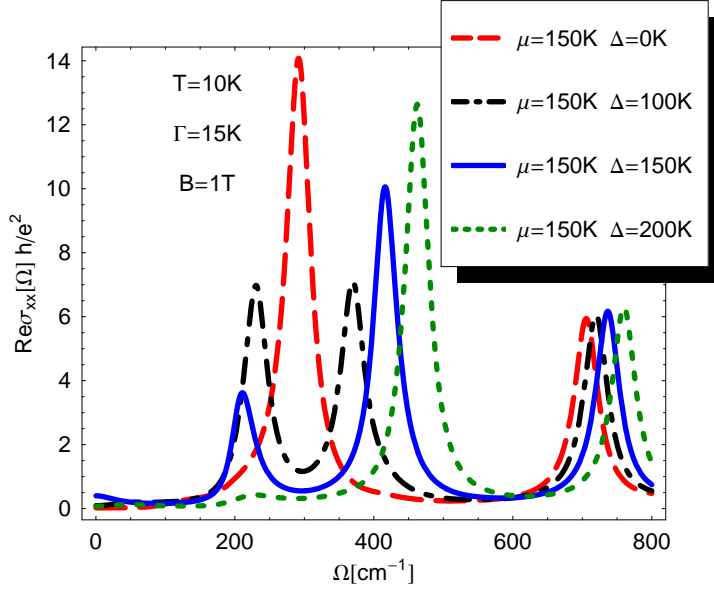


**Figure 4.** (Colour online) Real part of the longitudinal conductivity,  $\text{Re}\sigma_{xx}(\Omega)$  in units of  $e^2/h$  vs frequency  $\Omega$  in  $\text{cm}^{-1}$  for temperature  $T = 10\text{K}$ ,  $\Gamma = 15\text{K}$ ,  $B = 1\text{T}$  and chemical potential  $\mu = 150\text{K}$  for 4 values of the excitonic gap  $\Delta$ . Long dashed  $\Delta = 0\text{K}$ , dash-dotted  $\Delta = 100\text{K}$ , solid  $\Delta = 150\text{K}$ , short dashed  $\Delta = 200\text{K}$ .

The effect of an excitonic gap  $\Delta$  on the optical spectral weight distribution in a one Tesla magnetic field is illustrated in Fig. 4. Here as in the previous figures  $\Gamma = 15\text{K}$  and  $T = 10\text{K}$ . The chemical potential is set at  $150\text{K}$  in all cases. The long dashed (red), dash-dotted (black), solid (blue) and short dashed (green) curves are for  $\Delta = 0, 100\text{K}, 150\text{K}$  and  $200\text{K}$  respectively. The curve for  $\Delta = 0$  is for reference. We note that for finite  $\Delta = 100\text{K}$  the line at  $\Omega_1 = M_1(\Delta = 0) = 294\text{cm}^{-1}$  splits into two peaks [dash-dotted (black) curve]. The lower peak is at energy  $M_1(\Delta) - M_0(\Delta) = \sqrt{\Omega_1^2 + \Delta^2} - \Delta$ , while the upper peak is at  $M_1(\Delta) + M_0(\Delta) = \sqrt{\Omega_1^2 + \Delta^2} + \Delta$ . These two transitions for that value of chemical potential are illustrated in Fig. 2 middle frame (b) (see arrows). Additional transitions not shown in this frame can, of course, occur but these will have higher energy. For  $\Delta = 150\text{K} = \mu$  the  $n = 0$  state shown on the right hand cone of Fig. 2 (b) is occupied with a probability  $1/2$  at  $T = 0$ ,  $\Gamma = 0$  and a transition from  $n = 1$  lower cone to  $n = 0$  upper cone is possible as is from  $n = 0$  upper cone to  $n = 1$  of the same cone and each must be weighted by a factor  $1/2$ . The first has energy  $\sqrt{\Omega_1^2 + \Delta^2} + \Delta$ , while the second has energy  $\sqrt{\Omega_1^2 + \Delta^2} - \Delta$ . There is an additional transition coming from the second cone on the left hand side of the figure of energy  $\sqrt{\Omega_1^2 + \Delta^2} + \Delta$ . Thus the spectral intensity of the lower energy line in the solid curve (blue) is lower than that of the higher energy line by a factor of 3. Finally for  $\Delta = 200\text{K}$  ( $\Delta > \mu$ ) the energy of the lowest transition possible in both left and right side cones are the same equal to

$\sqrt{\Omega_1^2 + \Delta^2} + \Delta$  and so there is only one line in the dashed (green) curve. This pattern of behaviour should allow one to measure the occurrence of an excitonic gap catalyzed by the magnetic field. We note that the splitted peak in Fig. 4 with finite  $\Delta$  acquire a slight asymmetry because of the factor  $1 \pm \Delta^2/M_n M_{n+1}$  of Eq. (A.12) which is different for inter and intraband transitions.

So far we have shown the results for fixed values of chemical potential and magnetic field as a function of photon energy. It is also of interest to fix the photon frequency and sweep either chemical potential ( $\mu$ ) or field ( $B$ ) [32]. We begin with the first of these two possibilities and this is illustrated in Fig. 5. Four well chosen frequencies are selected,

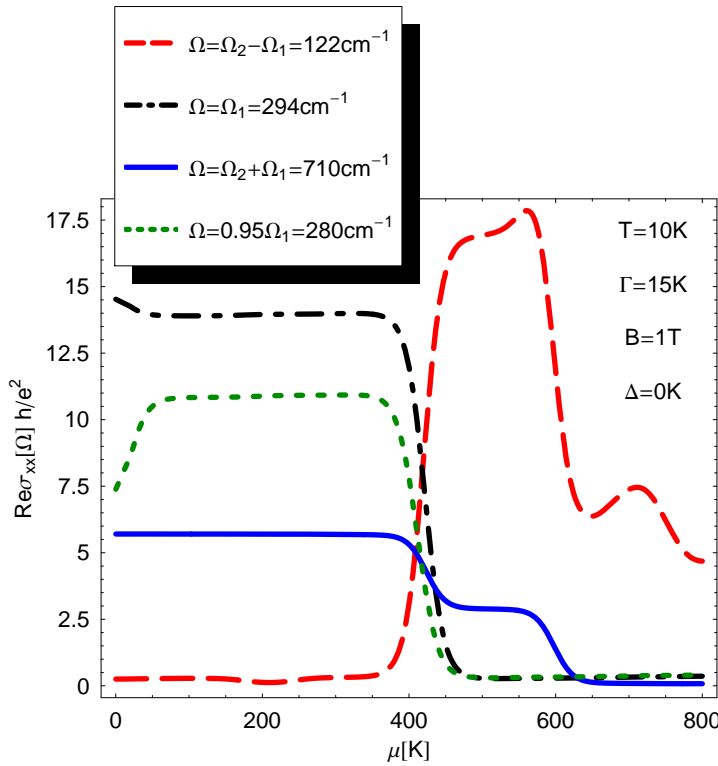


**Figure 5.** (Colour online) Real part of the longitudinal conductivity,  $\text{Re}\sigma_{xx}(\Omega)$  in units of  $e^2/h$  vs the chemical potential  $\mu$  in K for  $T = 10\text{K}$ ,  $\Gamma = 15\text{K}$ ,  $B = 1\text{T}$  and  $\Delta = 0$ . Four frequencies  $\Omega$  are considered, long dashed  $\Omega = 122\text{cm}^{-1}$ , dash-dotted  $\Omega = 294\text{cm}^{-1}$ , solid  $\Omega = 710\text{cm}^{-1}$ , short dashed  $\Omega = 0.95\Omega_1 = 280\text{cm}^{-1}$ . The first three frequencies correspond to  $\Omega = \Omega_2 - \Omega_1$ ,  $\Omega_1$  and  $\Omega_2 + \Omega_1$ , respectively, for the parameters used.

viz.  $\Omega = \Omega_2 - \Omega_1 = 122\text{cm}^{-1}$  long dashed curve (red),  $\Omega = \Omega_1 = 294\text{cm}^{-1}$  dash-dotted curve (black),  $\Omega = \Omega_2 + \Omega_1 = 710\text{cm}^{-1}$  solid curve (blue), and  $\Omega = 0.95\Omega_1 = 280\text{cm}^{-1}$  short dashed curve (green). Taking these in order, we note that the long dashed curve (red) is near zero until  $\mu$  reaches the value of 420K at which point it increases rapidly reaching a plateau at  $\text{Re}\sigma_{xx}(\Omega) \approx 17.5e^2/h$  [the height being set by the height of the peak in the solid (blue) curve in Fig. 1] after which it drops rapidly as  $\mu$  goes through 595K. It does not drop down all the way to zero however as it continues to sample

parts of the peaks at the difference in frequencies  $M_{n+1} - M_n$  until these move below the sampling optical frequency set at  $122\text{cm}^{-1}$ . The next optical frequency chosen at  $\Omega = \Omega_1$  short-long dashed (black) curve begins by sampling the equivalent curve in Fig. 1 where the peak has height  $\sim 14e^2/h$ . However when  $\mu$  crosses the energy of the first Landau level at  $420\text{K}$  this peak disappears and the curve drops to zero. No other level crosses this frequency again. The short dashed curve is for  $\Omega = 0.95\Omega_1$ . It shows very much the same behaviour as the previous case, but its plateau height is a little smaller because the peak (dash-dotted curve of Fig. 1) is sampled not at its center, but rather slightly below its maximum value. The final solid (blue) curve is for  $\Omega = \Omega_2 + \Omega_1$ . In this case a first plateau is seen at small  $\mu$  with height  $\sim 5.5e^2/h$  which is the height of the second peak in the dash-dotted (black) curve of Fig. 1. It drops to half of this value as  $\Omega$  crosses  $420\text{K}$  and then near zero as  $\Omega$  crosses  $595\text{K}$ . All features of these curves can be traced to the corresponding behaviour of the curves of Fig. 1. An additional feature of these curves is now described. Note that as the chemical potential gets small the black (dash-dotted) curve increases slightly, while the green (dotted) curve drops. As we have described in connection with Fig. 3 the line shapes do depend on the value of  $\mu$  if it falls within order  $\Gamma$  and/or  $T$  of a Landau level energy  $M_n$ . For  $\mu$  near zero, the first peak height in the black (dash-dotted) curve of Fig. 1 increases by  $\sim 5\%$  and its width is also slightly narrowed. This leads to a slight increase in peak height at  $\Omega = \Omega_1 = 294\text{cm}^{-1}$  monitored in the black (dash-dotted) curve of Fig. 5 and a reduction in the green (dotted) curve which monitors the height of the curve slightly off the peak at  $\Omega = 0.95\Omega_1 = 280\text{cm}^{-1}$ .

Another set of useful curves when considering possible experimental configurations is to fix the frequency of the light as well as the chemical potential and sweep the magnetic field. Results are shown in Fig. 6 for three cases  $\Omega = 200\text{cm}^{-1}$  long dashed (red) curve, dash-dotted (black) curve for  $\Omega = 400\text{cm}^{-1}$  and solid (blue) for  $\Omega = 800\text{cm}^{-1}$ . In all cases  $T = 10\text{K}$ ,  $\Gamma = 15\text{K}$ ,  $\mu = 50\text{K}$  and the excitonic gap  $\Delta$  is taken to be zero. On the horizontal axis we plotted  $1/\sqrt{B(\text{T})}$ , the inverse square root of the magnetic field in Tesla, so that fields below one tesla fall above one on this scale. The pattern of oscillations is perhaps more complex than in previous curves, but can easily be traced out from a knowledge of such curves for  $\text{Re } \sigma_{xx}(\Omega)$  at different values of  $B$ . As an example consider the case  $\Omega = 200\text{cm}^{-1}$ . The value of  $\text{Re } \sigma_{xx}(\Omega)h/e^2$  at  $1/\sqrt{B(\text{T})} = 1$  is just that of the dash-dotted (black) curve of Fig. 1 read at  $\Omega = 200\text{cm}^{-1}$ . As  $B$  is decreased from its value  $1\text{T}$ , the first peak in dash-dotted curve in Fig. 1 will move to lower frequency and so increases significantly the value of longitudinal conductivity at  $\Omega = 200\text{cm}^{-1}$ . Its peak will cross this reference energy for  $1/\sqrt{B(\text{T})} \simeq 1.47$  and this produces the first peak in the long dashed (red) curve of Fig. 6. As  $B$  is decreased further below one Tesla, the second peak in the dash-dotted curve of Fig. 1 will also move through  $\Omega = 200\text{cm}^{-1}$ . This occurs for  $1/\sqrt{B(\text{T})} \simeq 3.5$ , where a second lower intensity peak is seen in the long dashed (red) curve of Fig. 6. The other curves of Fig. 6 can be traced out from similar considerations based on Fig. 1 with attention paid to the evolution of these curves with changing value of  $B$ .



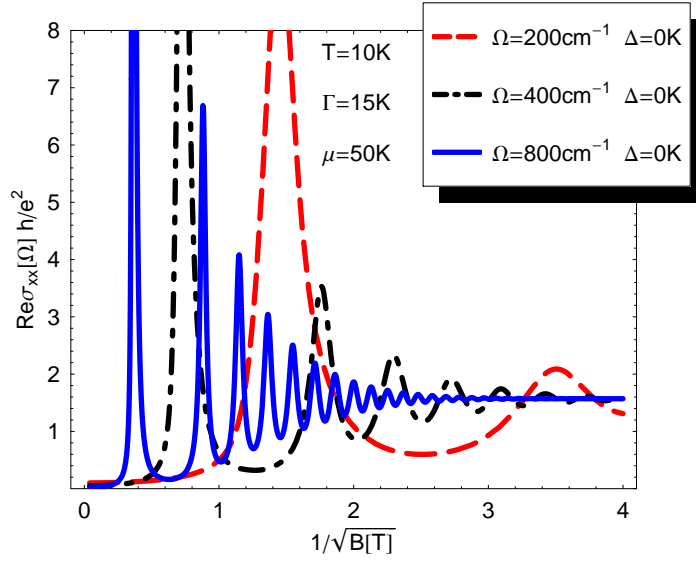


**Figure 6.** (Colour online) Real part of the longitudinal conductivity,  $\text{Re}\sigma_{xx}(\Omega)$  at three frequencies, long dashed  $200\text{cm}^{-1}$ , dash-dotted  $400\text{cm}^{-1}$ , solid  $800\text{cm}^{-1}$  as a function of the inverse of the square root of the magnetic field,  $1/\sqrt{B}$  with  $B$  in T. The other parameters are  $T = 10\text{K}$ ,  $\Gamma = 15\text{K}$  and  $\mu = 50\text{K}$ .

### 3.2. Spectral weight

An interesting quantity to consider is the optical spectral weight that falls between  $\Omega = 0$  and  $\Omega = \Omega_m$  with  $\Omega_m$  a variable upper limit in the integral

$$W(\Omega_m) = \int_0^{\Omega_m} d\Omega \text{Re}\sigma_{xx}(\Omega). \quad (26)$$

For the case  $T = \Gamma = \Delta = B = 0$  we have [16]

$$\sigma_{xx}(\Omega) = \frac{\pi e^2 N_f}{h} |\mu| \delta(\Omega) + \frac{\pi e^2 N_f}{4h} \theta\left(\frac{|\Omega|}{2} - |\mu|\right). \quad (27)$$

With  $N_f = 2$  this leads to

$$W(\Omega_m) = \frac{e^2}{h} (\pi|\mu| + \theta(\Omega_m/2 - |\mu|)\pi(\Omega_m/2 - |\mu|)) \simeq \frac{e^2 \pi \Omega_m}{h} \quad \text{for } \Omega_m \gg |\mu|. \quad (28)$$

For finite  $B$ , assuming for simplicity  $M_0 < \mu < M_1$  we get from Eq. (23)

$$\sigma_{xx}(\Omega) = \frac{e^2 N_f v_F^2 |eB|}{2c} \sum_{n=0}^{\infty} \frac{\delta(M_n + M_{n+1} - \Omega)}{M_n + M_{n+1}}. \quad (29)$$

Accordingly for  $\Delta = 0$

$$\begin{aligned} W(\Omega_m) &= \frac{e^2 N_f v_F^2 |eB|}{2c} \sum_{n=0}^{\infty} \frac{\theta(\Omega_m - M_n - M_{n+1})}{M_n + M_{n+1}} \\ &= \frac{\pi e^2}{h} \sqrt{2\hbar |eB| v_F^2 / c} \sum_{n=0}^N \frac{1}{\sqrt{n} + \sqrt{n+1}}. \end{aligned} \quad (30)$$

For large values  $\Omega_m$  the maximum  $N$  that contributes to (30) can be estimated from  $\Omega_m = M_N + M_{N+1} \simeq 2M_N$  and so  $N = \frac{\Omega_m^2}{8\hbar|eB|v_F^2/c}$ . But

$$\sum_{n=0}^N \frac{1}{\sqrt{n} + \sqrt{n+1}} = \sqrt{N+1} \approx \sqrt{N} \quad \text{for } N \gg 1, \quad (31)$$

and so

$$W(\Omega_m) \simeq \frac{e^2 \pi \Omega_m}{h} \frac{1}{2} \quad (32)$$

which agrees with Eq. (28) as we would expect. We note that as we have stated, the area under each line goes as  $\sqrt{B}$ , but the sum over the lines up to  $\Omega_m$  gives another factor  $\sim 1/\sqrt{B}$  which means that  $W(\Omega_m)$  is independent of  $B$ . In Fig. 7 we show

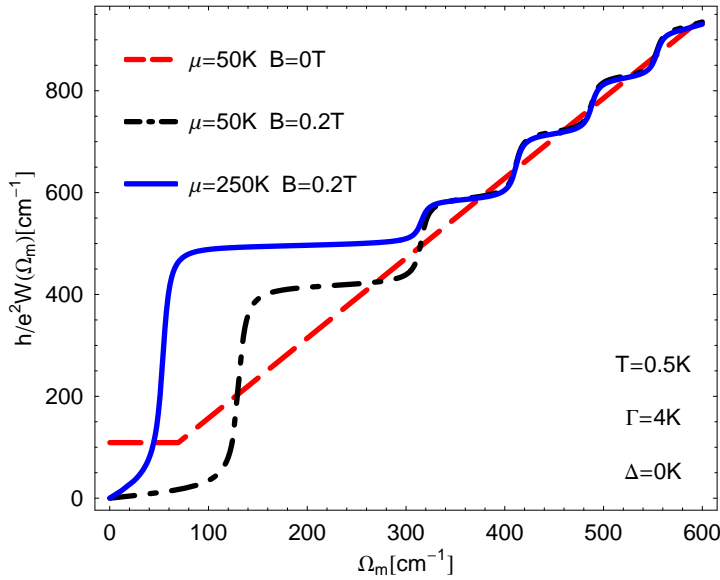


**Figure 7.** (Colour online) Variation of the optical sum  $W(\Omega_m)$  (multiplied by  $h/e^2$ ) in  $\text{cm}^{-1}$  as a function of  $\Omega_m$  in  $\text{cm}^{-1}$  for three different cases. Long dashed  $\mu = 50\text{K}$ ,  $B = 0\text{T}$  and  $T = \Gamma = 0\text{K}$  (see Eq. (28)); dash-dotted  $\mu = 50\text{K}$ ,  $B = 0.2\text{T}$ ,  $T = 0.5\text{K}$  and  $\Gamma = 4\text{K}$ ; solid  $\mu = 250\text{K}$ ,  $B = 0.2\text{T}$ ,  $T = 0.5\text{K}$  and  $\Gamma = 4\text{K}$ .

numerical results for  $(h/e^2)W(\Omega_m)$  in units of  $\text{cm}^{-1}$  as a function of  $\Omega_m$  is  $\text{cm}^{-1}$ . The long dashed (red) curve is computed on the base of the first equality in Eq. (28) for  $\mu = 50\text{K}$ ,  $T = 0\text{K}$ , and  $B = 0\text{T}$  and is given for comparison with the two other curves. These curves are obtained by numerical integration of Eq. (26) with  $\text{Re } \sigma_{xx}(\Omega)$  given by Eq. (A.12) for the case  $T = 0.5\text{K}$ ,  $\Gamma = 4\text{K}$ ,  $\Delta = 0$  and finite  $B = 0.2\text{T}$ . The dash-dotted (black) curve is for chemical potential  $\mu = 50\text{K}$ , while solid (blue) is for  $\mu = 250\text{K}$ . For the first case  $\mu$  is below  $M_1$  at  $131.5\text{cm}^{-1}$  and for the second is above. At small values of  $\Omega_m$  both curves start at zero and remain small until  $\Omega_m$  goes through the first Landau peak in Fig. 1 at which point it rises sharply and subsequently exhibits a plateau before showing a next sharp rise. For the dash-dotted curve (black) the first rise is at  $131.5\text{cm}^{-1}$  (interband line), but for the solid (blue) curve it is at the intraband

line ( $54.6 \text{ cm}^{-1}$ ). As  $\Omega_m$  increases to include several peaks in  $\sigma_{xx}(\Omega)$  the curves start to follow more closely the  $B = 0\text{T}$  result [long dashed (red) curve]. This behaviour can be understood better from a consideration of Eq. (30). The magnetic field mainly readjusts the available optical spectral weight among the Landau levels below  $\Omega_m$ .

To be specific we have considered explicitly in this section only the case  $M_0 < \mu < M_1$ . For  $\mu \in ]M_N, M_{N+1}[$  we can show that the missing spectral weight in the lines  $n \leq N$  is all to be found in the single intraband line at  $M_{N+1} - M_N$ . From Eq. (23) and noting Eqs. (24) and (25) as  $T \rightarrow 0$ , the optical spectral weight lost in units of  $(e^2/h)M_1(\pi/2)$  is

$$\sum_{n=0}^{N-1} \frac{2}{\sqrt{n+1} + \sqrt{n}} + \frac{1}{\sqrt{N+1} + \sqrt{N}} \equiv \frac{1}{\sqrt{N+1} - \sqrt{N}}. \quad (33)$$

The first term in the left hand side is the spectral weight from all the lines that have completely disappeared from  $n = 0$  to  $N - 1$ . The second term is from the reduction in intensity by a factor of 1/2 of the line at  $n = N$ . The quantity in the right hand side is the optical weight of the intraband line which has picked up all of the lost intensity.

### 3.3. Hall conductivity

Next we consider the absorptive part of the transverse Hall conductivity. The calculations are based on the equation (10). In Fig. 8 we show results for  $\text{Im } \sigma_{xy}(\Omega)$  in

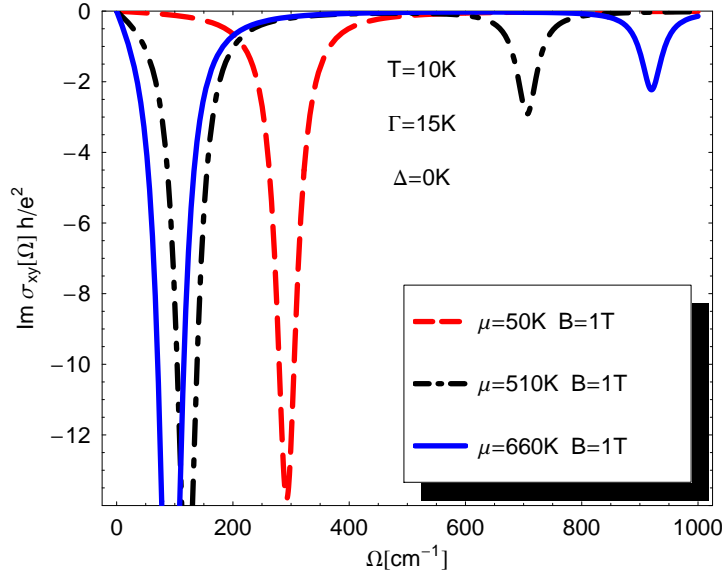


**Figure 8.** (Colour online) The imaginary part of the Hall conductivity,  $\text{Im } \sigma_{xy}(\Omega)$  in units of  $e^2/h$  as a function of frequency  $\Omega$  in  $\text{cm}^{-1}$ . The three cases are for  $\mu = 50\text{K}$  (long dashed),  $\mu = 510\text{K}$  (dash-dotted) and  $\mu = 660\text{K}$  (solid). The other parameters are  $B = 1\text{T}$ ,  $T = 10\text{K}$  and  $\Gamma = 15\text{K}$ .

units of  $e^2/h$  as a function of  $\Omega$  in  $\text{cm}^{-1}$ . In all cases considered temperature  $T = 10\text{K}$ ,

impurity scattering rate  $\Gamma = 15\text{K}$  and the excitonic gap  $\Delta = 0$ . The magnetic field  $B = 1\text{T}$  and three values of chemical potential are considered. The long dashed (red) curve is for  $\mu = 50\text{K}$  below the energy of the  $n = 1$  Landau level, dash-dotted (black)  $\mu = 510\text{K}$  between  $n = 1$  and  $n = 2$ , and solid (blue)  $\mu = 660\text{K}$  between  $n = 2$  and  $n = 3$  as in Fig. 1. We note a single peak in the long dashed (red) curve at  $M_1$  in contrast to two in the other two curves. For the dash-dotted (black) curve the peaks are at  $M_2 - M_1$  and  $M_1 + M_2$ , respectively, and for the solid (blue) curve they are at  $M_3 - M_2$  and  $M_2 + M_3$ . These features can be easily understood from Eq. (10) for  $\sigma_{xy}(\Omega)$  when we take its imaginary part in the limit  $\Delta = 0$ ,  $\Gamma \rightarrow 0$  which is for  $\Omega > 0$ ,  $\mu > 0$

$$\text{Im } \sigma_{xy}(\Omega) = -\frac{e^2}{h} M_1^2 \frac{\pi}{2} \sum_{n=0}^{\infty} [n_F(M_n) - n_F(M_{n+1}) - n_F(-M_{n+1}) + n_F(-M_n)] \quad (34)$$

$$\times \left[ \frac{\delta(\Omega - M_{n+1} + M_n)}{M_{n+1} - M_n} + \frac{\delta(\Omega - M_{n+1} - M_n)}{M_{n+1} + M_n} \right]. \quad (35)$$

Taking the limit of zero temperature,  $T = 0$  in Eq. (34) only the first two thermal factors in the square bracket survive. For  $\mu \in ]M_0, M_1[$  we get

$$\text{Im } \sigma_{xy}(\Omega) = -\frac{e^2}{h} M_1^2 \pi \frac{\delta(\Omega - M_1)}{M_1}, \quad (36)$$

while for  $\mu \in ]M_N, M_{N+1}[$  with  $N > 0$  we get

$$\text{Im } \sigma_{xy}(\Omega) = -\frac{e^2}{h} M_1^2 \frac{\pi}{2} \left[ \frac{\delta(\Omega - M_{N+1} - M_N)}{M_{N+1} + M_N} + \frac{\delta(\Omega - M_{N+1} + M_N)}{M_{N+1} - M_N} \right]. \quad (37)$$

Thus for  $\mu \in ]M_0, M_1[$  the transverse Hall conductivity exhibits a single peak at  $\Omega = M_1$  with weight  $2/M_1$ , in units of  $(e^2/h)(\pi/2)M_1^2$  and for  $\mu \in ]M_N, M_{N+1}[$  with  $N > 0$  it has two peaks at  $M_{N+1} + M_N$  and  $M_{N+1} - M_N$  with weight  $1/(M_{N+1} + M_N)$  and  $1/(M_{N+1} - M_N)$ , respectively. Thus the case  $\mu \in ]M_0, M_1[$  is different from all others. This distinguishes Dirac from a classical Landau level quantization, for which, all cases would have two peaks. Also the area under the peaks in  $\text{Im } \sigma_{xy}(\Omega)$  is  $\sim \sqrt{B}$  in analogy to what we found for  $\text{Re } \sigma_{xx}(\Omega)$ .

Next we consider the effect of a finite excitonic gap on the imaginary part of the Hall conductivity. In this case even for  $\Gamma \rightarrow 0$ ,  $\Omega > 0$ ,  $\mu > 0$  equation (10) is slightly more complicated than (34) because of the additional factors  $1 \pm \Delta^2/M_n M_{n+1}$  which are only equal to 1 when  $\Delta = 0$ . Nevertheless to understand physically the results given in Fig. 9 this extra complication is not needed and we can use Eq. (34) as a guide. What is most important is to look at the thermal factors. We will consider only the case when the chemical potential falls between  $n = 0$  and  $n = 1$  Landau level in energy. The relevant thermal factor is  $n_F(M_0) - n_F(M_1)$ . All four curves in Fig. 9 have  $\mu = 150\text{K}$ . The long dashed (red) curve is for  $\Delta = 0\text{K}$  and is included for reference. It shows a single peak (in  $-\text{Im } \sigma_{xy}(\Omega)$ ) at  $294\text{cm}^{-1}$  as we know from our previous discussion. For the dash-dotted (black) curve  $\Delta = 100\text{K}$  which falls below the value of chemical potential (see Fig. 2 (b)). In this case the thermal factors in Eq. (34) at  $T = 0$  give 1 and the delta functions correspond to  $\Omega = \sqrt{\Delta^2 + \Omega_1^2} - \Delta$  and  $\Omega = \sqrt{\Delta^2 + \Omega_1^2} + \Delta$ . Thus, the

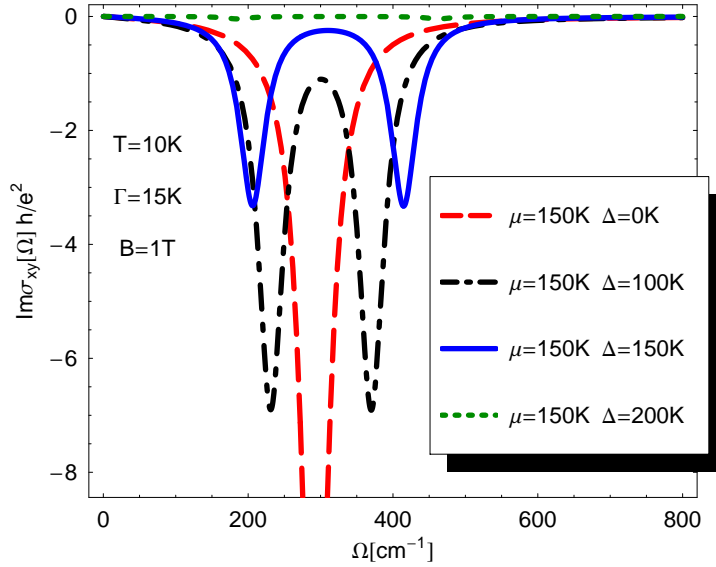


**Figure 9.** (Colour online) The imaginary part of the Hall conductivity,  $\text{Im} \sigma_{xy}(\Omega)$  in units of  $e^2/h$  vs frequency  $\Omega$  in  $\text{cm}^{-1}$  for temperature  $T = 10\text{K}$ ,  $\Gamma = 15\text{K}$ ,  $B = 1\text{T}$  and chemical potential  $\mu = 150\text{K}$  for 4 values of the excitonic gap  $\Delta$ . Long dashed  $\Delta = 0\text{K}$ , dash-dotted  $\Delta = 100\text{K}$ , solid  $\Delta = 250\text{K}$ , short dashed  $\Delta = 200\text{K}$ .

peak in the long dashed curve has split into two. Further such peak has approximately, but not exactly the same optical spectral weight as that under the single peak of long dashed line. This arises because of the weighting factors  $1 \pm \Delta^2/M_n M_{n+1}$  of Eq. (10) not shown explicitly in Eq. (34). For  $\Delta = \mu$  [solid (blue) curve] the two peaks remain at  $\Omega = \sqrt{\Delta^2 + \Omega_1^2} \pm \Delta$  (note the small shift which corresponds to the slightly different values of the gap between solid and short-long dashed curve). However, the thermal factor  $n_F(\Delta) - n_F(\Delta + \sqrt{\Delta^2 + \Omega_1^2})$  now equals  $1/2$  rather than  $1$  for the two previous cases, so that this feature on its own reduces the optical spectral weight of these peaks by half. Finally for the short dashed (green) curve the gap  $\Delta$  is larger than is the chemical potential and the thermal factor  $n_F(M_0) - n_F(M_1)$  is zero, so that no peak is seen.

In Fig. 10 we show results for the change in  $\text{Im} \sigma_{xy}(\Omega)$  in units of  $e^2/h$  as a function of  $\mu$  in Kelvin at fixed optical frequency. This figure is the analog of Fig. 5. The same parameters  $T = 10\text{K}$ ,  $\Gamma = 15\text{K}$ ,  $B = 1\text{T}$  and  $\Delta = 0$  are chosen as well as  $\Omega$ , namely, long dashed (red) curve,  $\Omega = \Omega_2 - \Omega_1 = 122\text{cm}^{-1}$ . The absorptive Hall conductivity for this curve is near zero until the first Landau level energy  $420\text{K}$  is crossed, where it drops below  $-17e^2/h$  after which it shows a plateau till the next level is crossed at  $\mu = 595\text{K}$ , where the second step is seen, etc. The dash-dotted (black) curve is for  $\Omega = \Omega_1 = 294\text{cm}^{-1}$ . In this case the first plateau is at  $\sim -14e^2/h$  till the energy of the  $n = 1$  Landau level is crossed in which case it drops to near zero value. The short dashed (green) curve is for  $\Omega = 0.95\Omega_1 = 280\text{cm}^{-1}$  and follows the dash-dotted (black) curve except the plateau is at  $\sim -10e^2/h$  as we expect. Finally the solid (blue) curve

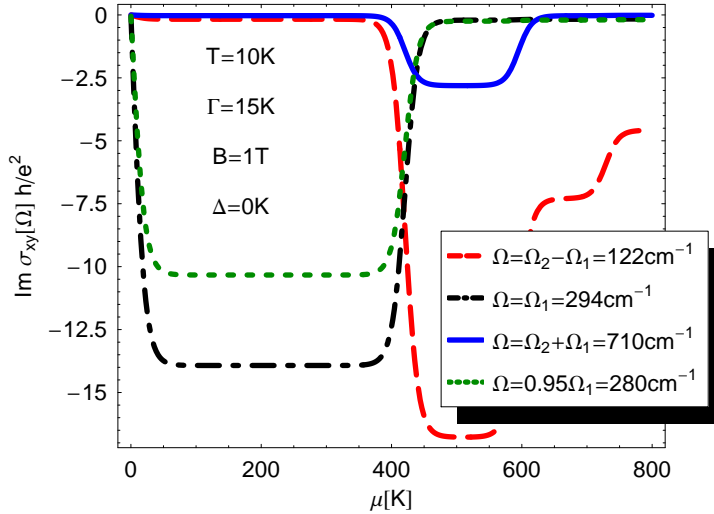


**Figure 10.** (Colour online) The imaginary part of the Hall conductivity,  $\text{Im } \sigma_{xy}(\Omega)$  in units of  $e^2/h$  as a function chemical potential  $\mu$  in K. Four frequencies are considered, long dashed  $\Omega = \Omega_2 - \Omega_1 = 122\text{cm}^{-1}$ , dash-dotted  $\Omega = \Omega_1 = 294\text{cm}^{-1}$ , solid  $\Omega = \Omega_2 + \Omega_1 = 710\text{cm}^{-1}$  and short dashed  $\Omega = 0.95\Omega_1 = 280\text{cm}^{-1}$ . The other parameters are  $B = 1\text{T}$ ,  $T = 10\text{K}$  and  $\Gamma = 15\text{K}$ .

is for  $\Omega = \Omega_1 + \Omega_2 = 710\text{cm}^{-1}$ . It starts at zero till  $\mu$  crosses 420K at which point it shows a step down, remains nearly constant and finally steps back to near zero value at  $\mu = 595\text{K}$  as expected from consideration of Fig. 8.

The final Fig. 11 shows results for the variation of  $\text{Im } \sigma_{xy}(\Omega)$  in units of  $e^2/h$  vs the inverse square root of the magnetic field,  $1/\sqrt{B(T)}$ . Here temperature  $T = 10\text{K}$ , impurity scattering rate  $\Gamma = 15\text{K}$  and the chemical potential  $\mu = 50\text{K}$  with excitonic gap  $\Delta = 0$ . Three optical frequencies are chosen: long dashed (red) curve  $\Omega = 160\text{cm}^{-1}$ , dash-dotted (black) curve  $\Omega = 240\text{cm}^{-1}$  and solid (blue) curve  $\Omega = 400\text{cm}^{-1}$ . These curves are similar to those of Fig. 6 for the longitudinal case, but here exhibit only a single peak as is expected from the curves shown in Fig. 8.

#### 4. Discussion

In this paper we have extended the calculation of the ac conductivity of graphene presented in Ref. [8] in several ways. One emphasis has been on presenting results for different values of the chemical potential,  $\mu$ . In a field-effect device,  $\mu$  can be varied within the range of a few thousands of Kelvin by changing the gate voltage [1, 2, 3, 17]. This implies that for fields of the order of 1T,  $\mu$  can be made to sweep over several Landau levels. Recently [18] infrared spectroscopy has been successfully applied to study FET devices based on poly(3-hexylthiophene). We find a rich pattern of behaviour for the  $\Omega$  dependence of the real (absorptive) part of the diagonal conductivity,  $\text{Re } \sigma_{xx}(\Omega, T)$  as a function of  $\Omega$  in a fixed external magnetic field oriented perpendicular to the

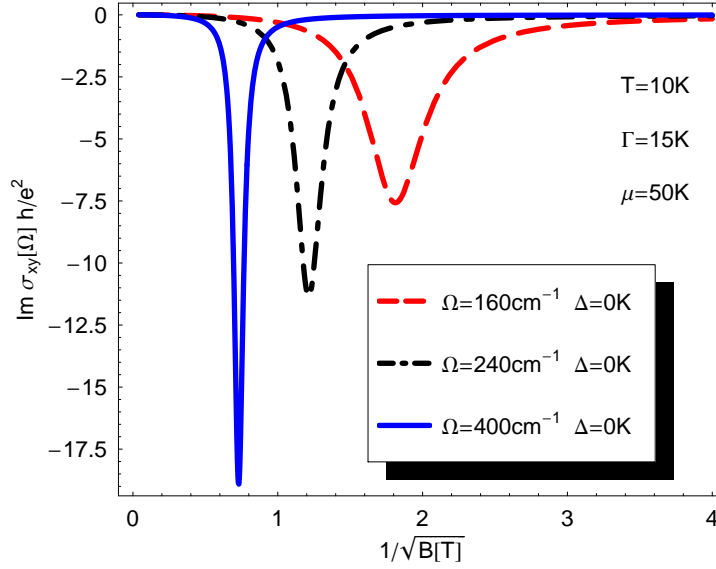


**Figure 11.** (Colour online) The imaginary part of the Hall conductivity,  $\text{Im } \sigma_{xy}(\Omega)$  in units of  $e^2/h$  as a function of the inverse of the square root of the magnetic field,  $1/\sqrt{B}$  with  $B$  in T. Three frequencies are considered, long dashed  $160\text{cm}^{-1}$ , dash-dotted  $240\text{cm}^{-1}$ , solid  $400\text{cm}^{-1}$ . The other parameters are  $T = 10\text{K}$ ,  $\Gamma = 15\text{K}$  and  $\mu = 50\text{K}$ .

graphene sheet. Peaks are seen in  $\sigma_{xx}(\Omega, T)$  corresponding to the possible transition between Landau levels from the hole to particle band (interband) or within a given cone (intraband). For  $\mu$  between the  $n = 0$  and  $n = 1$  levels there are lines at  $\Omega = M_1$ ,  $M_1 + M_2$ ,  $M_2 + M_3$  (interband), etc., where  $M_i$  is the position in energy of the  $i$ -th Landau level. There is no peak below  $M_1$ . The relative optical spectral weight between the various levels decay approximately as  $1/\Omega$  with  $\Omega$  evaluated at the center of each peak. When the chemical potential falls between the energy of the  $n = 1$  and  $n = 2$  level the peak at  $\Omega = M_1$  fades into the background and a new line appears at the lower frequency  $M_2 - M_1$  (intraband). In addition, the intensity of the line at  $M_1 + M_2$  drops to half its value, while all other lines remain the same. As the chemical potential crosses higher and higher Landau level, say falls between  $M_N$  and  $M_{N+1}$ , the low energy peak has shifted to  $M_{N+1} - M_N$  (intraband) after which all peaks previously seen have disappeared into background except for the one at  $M_{N+1} + M_N$  which has half its previous intensity. Again all peaks above this energy remain unaltered. The peculiar behaviour of the peak at  $\Omega = M_1$  which is either present with full intensity or completely absent is the hallmark of Dirac as oppose to Schrödinger behaviour. This peak can be classified either as inter or intra when the excitonic gap  $\Delta = 0$ , an ambiguity that is lifted for  $\Delta \neq 0$ . For Landau levels based on the Schrödinger equation the interband lines are evenly spaced while the intraband line is fixed in energy, and all interband lines first half their intensity before disappearing entirely as  $\mu$  is increased.

We have found that the transition from one configuration of absorption lines to

another occurs for a small change in chemical potential near a given Landau level energy with the scale for the incremental change in  $\mu$  set by temperature and/or level broadening  $\Gamma$ . Away from these special values of  $\mu$  the curves do not change significantly.

In anticipation of experiments [32] we also provide scans of the the behaviour of  $\text{Re } \sigma_{xx}(\Omega, T)$  at fixed  $\Omega$  as a function of chemical potential or of magnetic field. The pattern of behaviour found is traced back to that just described for  $\text{Re } \sigma_{xx}(\Omega, T)$  vs  $\Omega$  at different values of field and chemical potential. Parallel results for the absorptive part of the transverse Hall conductivity are also presented.

The possibility that an excitonic gap may open in graphene under high magnetic field has been considered by many authors [19, 20, 21, 24] and may even have been observed in recent experiments [23]. We have considered its effect on the absorption peak seen in both diagonal and Hall conductivity. Our specific predictions are that, a given peak can split into two, can disappear entirely or can simply shift to higher energy without splitting depending on the value of the chemical potential. In some circumstances the optical spectral weight under the splitted peak can differ from each other by a factor of order 3.

Many of the results shown in the figures were obtained on the basis of general formulas for the conductivity, but it was found that simplified versions which can be more easily used to interpret experimental results are surprisingly accurate in the cases considered. They involve sums over Landau level indices of Lorentzian forms. Recently Li *et al.* [22] and Sadowski *et al.* [29] used related forms to analyze their results.

Early magnetorefectance data [33] in magnetic fields in the range 1 to 10 T carried out in graphite assigned lines to the  $H$ -point and some of these lines were found to follow a square root of  $B$  law as expected for graphene. Recent data of Ref. [22] at higher fields up to 20 T, however, found a conventional linear in  $B$  behaviour. Very recent infrared transmission data [29] in ultrathin epitaxial graphite [30, 31] in fields up to 4 T do show  $\sqrt{B}$  law and these authors took this to be evidence that their carbon sheets are sufficiently decoupled to behave like graphene. However, this interpretation also requires that they assume that various sheets carry different charges, i.e. have different values of chemical potential. Nevertheless, the main lines seen in these data were assigned to the first three Dirac interband transitions and the  $(0, 1)$  intraband transition on the basis of their position in energy. They were also seen to vary in optical spectral weight as the square root of the magnetic field in good agreement with the findings in this work. Many other detailed predictions made in this paper have yet to be verified and should help in firmly establishing the special characteristic of quasiparticles in graphene.

## Acknowledgments

We thank D. Basov for sharing Ref. [22] prior to publication and E.J. Nicol for discussion. The work of V.P.G. was supported by the SCOPES-project IB7320-110848 of the Swiss NSF and by Ukrainian State Foundation for Fundamental Research. J.P.C. and S.G.Sh. were supported by the Natural Science and Engineering Research Council of Canada



(NSERC) and by the Canadian Institute for Advanced Research (CIAR).

### Appendix A. Calculation of $\sigma_{\pm}(\Omega)$ in magneto-optical Lorentzian model

We consider the complex conductivity  $\sigma_{\pm}(\Omega) = \sigma_{xx}(\Omega) \pm i\sigma_{xy}(\Omega)$ . Substituting the spectral function (3) in Eq. (2) after evaluating  $\text{tr}$  and integrating over momentum  $\mathbf{k}$  [see Appendix A of Ref. [8]] one obtains

$$\sigma_{\pm}(\Omega) = \frac{e^2 N_f v_F^2 |eB|}{4\pi c \Omega i} \int_{-\infty}^{\infty} d\omega d\omega' \frac{n_F(\omega') - n_F(\omega)}{\omega - \omega' - \Omega - i0} [\psi_1(\omega, \omega') \mp \text{sgn}(eB)\psi_2(\omega, \omega')], \quad (\text{A.1})$$

where the functions  $\psi_1(\omega, \omega')$  and  $\psi_2(\omega, \omega')$  are:

$$\psi_{1,2}(\omega, \omega') = \sum_{n,m=0}^{\infty} (-1)^{n+m+1} (\delta_{n,m-1} \pm \delta_{m,n-1}) \psi_{n,m}(\omega, \omega') \quad (\text{A.2})$$

with

$$\begin{aligned} \psi_{n,m}(\omega, \omega') &= \left(1 - \frac{\Delta^2}{M_n M_m}\right) (A_n(\omega)A_m(\omega') + B_n(\omega)B_m(\omega')) \\ &+ \left(1 + \frac{\Delta^2}{M_n M_m}\right) (A_n(\omega)B_m(\omega') + B_n(\omega)A_m(\omega')), \end{aligned} \quad (\text{A.3})$$

and

$$A_n(\omega) = \frac{\Gamma_n}{\pi[(\omega - M_n)^2 + \Gamma_n^2]}, \quad B_n(\omega) = \frac{\Gamma_n}{\pi[(\omega + M_n)^2 + \Gamma_n^2]}. \quad (\text{A.4})$$

One can easily check that

$$\psi_1(\omega, \omega') = \psi_1(\omega', \omega), \quad \psi_2(\omega, \omega') = -\psi_2(\omega', \omega). \quad (\text{A.5})$$

Using this symmetry one can rewrite Eq. (A.1) in the form

$$\begin{aligned} \sigma_{\pm}(\Omega) &= -\frac{e^2 N_f v_F^2 |eB|}{4\pi c \Omega i} \int_{-\infty}^{\infty} d\omega n_F(\omega) \int_{-\infty}^{\infty} d\omega' \left\{ \left[ \frac{1}{\omega - \omega' + \Omega + i0} + \frac{1}{\omega - \omega' - \Omega - i0} \right] \psi_1(\omega, \omega') \right. \\ &\left. \pm \text{sgn}(eB) \left[ \frac{1}{\omega - \omega' + \Omega + i0} - \frac{1}{\omega - \omega' - \Omega - i0} \right] \psi_2(\omega, \omega') \right\}. \end{aligned} \quad (\text{A.6})$$

Now using Eq. (A.2) we obtain

$$\begin{aligned} \sigma_{\pm}(\Omega) &= -\frac{e^2 N_f v_F^2 |eB|}{4\pi c \Omega i} \sum_{n,m=0}^{\infty} (-1)^{n+m+1} \int_{-\infty}^{\infty} d\omega n_F(\omega) \int_{-\infty}^{\infty} d\omega' \psi_{n,m}(\omega, \omega') \\ &\times \left\{ \left[ \frac{1}{\omega - \omega' + \Omega + i0} + \frac{1}{\omega - \omega' - \Omega - i0} \right] (\delta_{n,m-1} + \delta_{m,n-1}) \right. \\ &\left. \pm \text{sgn}(eB) \left[ \frac{1}{\omega - \omega' + \Omega + i0} - \frac{1}{\omega - \omega' - \Omega - i0} \right] (\delta_{n,m-1} - \delta_{m,n-1}) \right\}. \end{aligned} \quad (\text{A.7})$$

For a typical integral over  $\omega'$  we have

$$\begin{aligned} \int_{-\infty}^{\infty} \frac{d\omega' \psi_{n,m}(\omega, \omega')}{\omega - \omega' + \Omega + i0} &= \left(1 - \frac{\Delta^2}{M_n M_m}\right) \left( \frac{A_n(\omega)}{\omega - M_m + \Omega + i\Gamma_m} + \frac{B_n(\omega)}{\omega + M_m + \Omega + i\Gamma_m} \right) \\ &+ \left(1 + \frac{\Delta^2}{M_n M_m}\right) \left( \frac{B_n(\omega)}{\omega - M_m + \Omega + i\Gamma_m} + \frac{A_n(\omega)}{\omega + M_m + \Omega + i\Gamma_m} \right). \end{aligned} \quad (\text{A.8})$$

If the thermal factor  $n_F$  is absent, further integration over  $\omega$  would give an exact result:

$$\int_{-\infty}^{\infty} d\omega d\omega' \frac{\psi_{n,m}(\omega, \omega')}{\omega - \omega' + \Omega + i0} = \quad (\text{A.9})$$

$$\left(1 - \frac{\Delta^2}{M_n M_m}\right) \left(\frac{1}{M_n - M_m + \Omega + i(\Gamma_n + \Gamma_m)} + \frac{1}{-M_n + M_m + \Omega + i(\Gamma_n + \Gamma_m)}\right)$$

$$+ \left(1 + \frac{\Delta^2}{M_n M_m}\right) \left(\frac{1}{-M_n - M_m + \Omega + i(\Gamma_n + \Gamma_m)} + \frac{1}{M_n + M_m + \Omega + i(\Gamma_n + \Gamma_m)}\right).$$

In case we integrate with a smooth function  $n_F(\omega)$  we can approximately write

$$\int_{-\infty}^{\infty} d\omega n_F(\omega) \int_{-\infty}^{\infty} \frac{d\omega' \psi_{n,m}(\omega, \omega')}{\omega - \omega' + \Omega + i0} \simeq \quad (\text{A.10})$$

$$\left(1 - \frac{\Delta^2}{M_n M_m}\right) \left(\frac{n_F(M_n)}{M_n - M_m + \Omega + i(\Gamma_n + \Gamma_m)} + \frac{n_F(-M_n)}{-M_n + M_m + \Omega + i(\Gamma_n + \Gamma_m)}\right)$$

$$+ \left(1 + \frac{\Delta^2}{M_n M_m}\right) \left(\frac{n_F(-M_n)}{-M_n - M_m + \Omega + i(\Gamma_n + \Gamma_m)} + \frac{n_F(M_n)}{M_n + M_m + \Omega + i(\Gamma_n + \Gamma_m)}\right).$$

Similarly, taking the complex conjugate and changing  $\Omega \rightarrow -\Omega$ , we have

$$\int_{-\infty}^{\infty} d\omega n_F(\omega) \int_{-\infty}^{\infty} \frac{d\omega' \psi_{n,m}(\omega, \omega')}{\omega - \omega' - \Omega - i0} \simeq \quad (\text{A.11})$$

$$\left(1 - \frac{\Delta^2}{M_n M_m}\right) \left(\frac{n_F(M_n)}{M_n - M_m - \Omega - i(\Gamma_n + \Gamma_m)} + \frac{n_F(-M_n)}{-M_n + M_m - \Omega - i(\Gamma_n + \Gamma_m)}\right)$$

$$+ \left(1 + \frac{\Delta^2}{M_n M_m}\right) \left(\frac{n_F(-M_n)}{-M_n - M_m - \Omega - i(\Gamma_n + \Gamma_m)} + \frac{n_F(M_n)}{M_n + M_m - \Omega - i(\Gamma_n + \Gamma_m)}\right).$$

Hence we arrive at

$$\sigma_{\pm}(\Omega) = -\frac{e^2 N_f v_F^2 |eB|}{4\pi c \Omega i} \quad (\text{A.12})$$

$$\times \sum_{n=0}^{\infty} \left\{ \left(1 - \frac{\Delta^2}{M_n M_{n+1}}\right) [[n_F(M_n) - n_F(M_{n+1})] + [n_F(-M_{n+1}) - n_F(-M_n)]] \right.$$

$$\times \left[ \frac{1}{M_n - M_{n+1} + \Omega + i(\Gamma_n + \Gamma_{n+1})} + \frac{1}{M_n - M_{n+1} - \Omega - i(\Gamma_n + \Gamma_{n+1})} \right]$$

$$- \left(1 + \frac{\Delta^2}{M_n M_{n+1}}\right) [[n_F(-M_{n+1}) - n_F(M_n)] + [n_F(-M_n) - n_F(M_{n+1})]]$$

$$\times \left[ \frac{1}{M_n + M_{n+1} - \Omega - i(\Gamma_n + \Gamma_{n+1})} + \frac{1}{M_n + M_{n+1} + \Omega + i(\Gamma_n + \Gamma_{n+1})} \right]$$

$$\pm \text{sgn}(eB) \left[ \left(1 - \frac{\Delta^2}{M_n M_{n+1}}\right) [[n_F(M_n) - n_F(M_{n+1})] - [n_F(-M_{n+1}) - n_F(-M_n)]] \right.$$

$$\times \left[ \frac{1}{M_n - M_{n+1} + \Omega + i(\Gamma_n + \Gamma_{n+1})} - \frac{1}{M_n - M_{n+1} - \Omega - i(\Gamma_n + \Gamma_{n+1})} \right]$$

$$+ \left(1 + \frac{\Delta^2}{M_n M_{n+1}}\right) [[n_F(-M_{n+1}) - n_F(M_n)] - [n_F(-M_n) - n_F(M_{n+1})]]$$

$$\times \left[ \frac{1}{M_n + M_{n+1} - \Omega - i(\Gamma_n + \Gamma_{n+1})} - \frac{1}{M_n + M_{n+1} + \Omega + i(\Gamma_n + \Gamma_{n+1})} \right] \left. \right\},$$

where only the sum over  $n$  remained.

We verified that  $\text{Re } \sigma_{xx}(\Omega)$  computed for  $\Gamma_n(\omega) = \text{const}$  from the more approximate Eq. (A.12) agrees quantitatively with the results obtained from a full Eq. (7). This agreement is best for the resonance peaks and only small deviations are seen for  $\Omega \sim 0$ . Nevertheless, Eq. (A.12) has a few drawbacks due to approximations made in Eqs. (A.10), (A.11).

In particular, the Drude form cannot be recovered in  $B \rightarrow 0$  limit, while it can be obtained [8, 16] from an exact representation (7). Moreover, the imaginary parts of the diagonal conductivity,  $\text{Im}\sigma_{xx}(\Omega)$  and the Hall conductivity,  $\text{Im}\sigma_{xy}(\Omega)$  are divergent in the limit  $\Omega \rightarrow 0$  and do not satisfy Kramers-Kronig relations with the corresponding real parts found from Eq. (A.12). To correct these problems we move the term  $1/\Omega$  under the sum replacing it by its value at the pole of the corresponding denominator in Eq. (A.12) and arrive at Eqs. (9) and (10).

- [1] Novoselov K S, Geim A K, Morozov S V, Jiang D, Katsnelson M I, Grigorieva I V, Dubonos S V, Firsov A A 2005 *Nature* **438** 197
- [2] Zhang Y, Tan Y-W, Stormer H L, Kim P 2005 *Nature* **438** 201
- [3] Novoselov K S, Geim A K, Morozov S V, Jiang D, Zhang Y, Dubonos S V, Grigorieva I V, and Firsov A A 2004 *Science* **306** 666; Novoselov K S, Jiang D, Booth T, Khotkevich V V, Morozov S M, and Geim A K 2005 *Proc. Nat. Acad. Sc.* **102** 10451
- [4] Semenoff G W 1984 *Phys. Rev. Lett.* **53** 2449
- [5] DiVincenzo D P and Mele E J 1984 *Phys. Rev. B* **29** 1685
- [6] Zheng Y and Ando T 2002 *Phys. Rev. B* **65** 245420
- [7] Gusynin V P and Sharapov S G 2005 *Phys. Rev. Lett.* **95** 146801
- [8] Gusynin V P and Sharapov S G 2006 *Phys. Rev. B* **73** 245411
- [9] Peres N M R, Guinea F, and Castro Neto A H 2006 *Phys. Rev. B* **73** 125411
- [10] Castro Neto A H, Guinea F, and Peres N M R 2006 *Phys. Rev. B* **73** 205408
- [11] Sharapov S G, Gusynin V P, and Beck H 2004 *Phys. Rev. B* **69** 075104
- [12] Luk'yanchuk I A and Kopelevich Y 2004 *Phys. Rev. Lett.* **93** 166402
- [13] The fact that the phase shift of  $\pi$  in graphite is related to nonzero Berry's phase was discussed in Mikitik G P and Sharlai Yu V 1999 *Phys. Rev. Lett.* **82** 2147, *Phys. Rev. B* 2006 **73** 235112, see also Kosevich A M 2004 *Low Temp. Phys.* **30** 97 [*Fiz. Niz. Temp.* 2004 **30** 135] for a review.
- [14] Gusynin V P and Sharapov S G 2005 *Phys. Rev. B* **71** 125124
- [15] Ando T, Zheng Y, and Suzuura H 2002 *J. Phys. Soc. Jpn.* **71** 1318
- [16] Gusynin V P, Sharapov S G, and Carbotte J P 2006 *Phys. Rev. Lett.* **96** 256802
- [17] Bunch J S, Yaish Y, Brink M, Bolotin K, and McEuen P L 2005 *Nano Letters* **5** 287
- [18] Li Z Q, Wang G M, Sai N, Moses D, Martin M C, Di Ventra M, Heeger A J, and Basov D N 2006 *Nano Letters* **6** 224
- [19] Khveshchenko D V 2001 *Phys. Rev. Lett.* **87** 206401; Khveshchenko D V and H. Leal *Nucl. Phys. B* 2004 **687** 323
- [20] Khveshchenko D V 2001 *Phys. Rev. Lett.* **87** 246802
- [21] Gorbar E V, Gusynin V P, Miransky V A, and Shovkovy I A 2002 *Phys. Rev. B* **66** 045108
- [22] Li Z Q, Padilla W J, Tsai S-W, Dordevic S V, Burch K S, Wang Y J, and Basov D N 2006 *Phys. Rev. B* **74** 195404
- [23] Zhang Y, Jiang Z, Small J P, Purewal M S, Tan Y-W, Fazlollahi M, Chudow J D, Jaszczak J A, Stormer H L, Kim P 2006 *Phys. Rev. Lett.* **96** 136806
- [24] Gusynin V P, Miransky V A, Sharapov S G, and Shovkovy I A 2006 *Phys. Rev. B* **74** 195429. See also Ref. [21] for an earlier work.
- [25] Geim A K, private communication.
- [26] Lax B and Mavroides J C, in *Semiconductors and Semimetals Vol. 3*, edited by Willardson R K

- and Beer A C (Academic Press, New York and London, 1967), pp. 321-401.
- [27] Falkovsky L A and Varlamov A A 2006 cond-mat/0606800
  - [28] Gusynin V P, Sharapov S G and Carbotte J P 2006, cond-mat/0607727
  - [29] Sadowski M L, Martinez G, Potemski M, Berger C, and de Heer W A 2006 cond-mat/0605739, to appear in *Phys. Rev. Lett.*
  - [30] Berger C, Song Z, Li T, Li X, Ogbazghi A Y, Feng R, Dai Z, Marchenkov A N, Conrad E H, First P N, and de Heer W A 2004 *J. Phys. Chem. B* **108** 19912
  - [31] Berger C, Song Z, Li X, Wu X, Brown N, Naud C, Mayou D, Li T, Hass J , Marchenkov A N, Conrad E H, First P N, and de Heer W A 2006 *Science* **312** 1191
  - [32] Basov D N, private communication.
  - [33] Toy W W, Dresselhaus M S, and Dresselhaus G 1977 *Phys. Rev. B* **15** 4077